J. Fluid Mech. (2000), *vol.* 416, *pp.* 75–116. Printed in the United Kingdom

A numerical study of strained three-dimensional wall-bounded turbulence

By G. N. COLEMAN[1]†, J. KIM[1] AND P. R. SPALART[2]

[1]Mechanical and Aerospace Engineering Department, UCLA, 48-121 Engr. IV, Box 951597, Los Angeles, CA 90095-1597, USA

[2]Boeing Commercial Airplanes, PO Box 3707, Seattle, WA 98124-2207, USA

(Received 22 July 1999 and in revised form 6 March 2000)

Channel flow, initially fully developed and two-dimensional, is subjected to mean strains that emulate the effect of rapid changes of streamwise and spanwise pressure gradients in three-dimensional boundary layers, ducts, or diffusers. As in previous studies of homogeneous turbulence, this is done by deforming the domain of a direct numerical simulation (DNS); here however the domain is periodic in only two directions and contains parallel walls. The velocity difference between the inner and outer layers is controlled by accelerating the channel walls in their own plane, as in earlier studies of three-dimensional channel flows. By simultaneously moving the walls and straining the domain we duplicate both the inner and outer regions of the spatially developing case. The results are used to address basic physics and modelling issues. Flows subject to impulsive mean three-dimensionality with and without the mean deceleration of an adverse pressure gradient (APG) are considered: strains imitating swept-wing and pure skewing (sideways turning) three-dimensional boundary layers are imposed. The APG influences the structure of the turbulence, measured for example by the ratio of shear stress to kinetic energy, much more than does the pure skewing. For both deformations, the evolution of the Reynolds stress is profoundly affected by changes to the velocity–pressure-gradient correlation Π_{ij}. This term – which represents the finite time required for the mean strain to modify the shape and orientation of the turbulent motions – is primarily responsible for the difference (lag) in direction between the mean shear and the turbulent shear stresses, a well-known feature of perturbed three-dimensional boundary layers. Files containing the DNS database and model-testing software are available from the authors for distribution, as tools for future closure-model testing.

1. Introduction

The subject of this study is turbulent three-dimensional boundary layers (3DBLs), that is boundary layers with mean velocity profiles that change direction with distance from the surface. As a consequence, the mean velocity and mean vorticity are not everywhere orthogonal as they are in two-dimensional boundary layers. Our objective is to better understand the non-equilibrium case, where the 3DBL is created by an abrupt mean-flow perturbation. (We shall use 'perturbed' and 'non-stationary' as synonyms for the traditional meaning of non-equilibrium, to describe a flow subjected to a rapid change of the mean field to which the turbulence has not yet adjusted.)

† Present address: School of Engineering Sciences, Aeronautics and Astronautics, University of Southampton, Highfield, Southampton SO17 1BJ, UK.

These flows are abundant in both meteorology and engineering (Smits & Wood 1985). Although stationary 3DBLs (such as the Ekman layer) are not without importance and physical complexity (see e.g. Spalart 1989; Littell & Eaton 1994; Wu & Squires 1997; Coleman 1999), it is the transient response of the turbulence to an impulsively imposed mean deformation that is the most challenging to understand, and is the subject of this investigation. Specifically, we examine the transition of a statistically stationary two-dimensional incompressible turbulent flow to non-stationary states created by sudden application of three-dimensional mean strains. The focus here is upon the resulting statistics (rather than the behaviour of the instantaneous coherent-structures†), with an eye toward improving the performance of one-point turbulence models. Similar, less thorough, presentations of this work have appeared in Coleman, Kim & Spalart (1996*b*, 1997).

Since turbulence is inherently unsteady and three-dimensional, it might seem reasonable to assume that the three-dimensionality of the mean flow is irrelevant. Turbulence in perturbed 3DBLs would then be a simple extension of that found in stationary two-dimensional or three-dimensional boundary layers. It is not. There is now abundant evidence that suddenly adding mean three-dimensionality to a flow alters its character. (Reviews of stationary and perturbed turbulent 3DBL experiments and simulations can be found in Fernholz & Vagt 1981; van den Berg *et al.* 1988; Schwarz & Bradshaw 1994; Eaton 1995; or Johnston & Flack 1996). As an example, when a fully developed two-dimensional boundary layer is suddenly subjected to a spanwise mean shear by the impulsive motion of the surface, the flow often experiences a decrease of turbulent shear stress and drag (Moin *et al.* 1990; Jung, Mangiavacchi & Akhavan 1992; Laadhari, Skandaji & Morel 1994; Coleman, Kim & Le 1996*a*). Because addition of mean shear usually causes the turbulence to become more energetic, this behaviour is difficult to explain (and predict). We hope to clarify this phenomenon.

When the crossflow appears not because of applied surface shear but as the result of a spanwise pressure gradient, such as that found in a curved duct, upstream of a blunt obstacle, or over a swept wing, the 'streamwise component' of turbulent shear stress, $-\overline{u'v'}$, near the wall again tends to decrease (Bradshaw & Pontikos 1985); away from the surface, however, the stress typically increases (Pierce & Duerson 1975; Anderson & Eaton 1989; Schwarz & Bradshaw 1994; Ölçmen & Simpson 1995), presumably due to the outer-layer deformation associated with the mean streamwise pressure gradient. (More on this point below.) The suddenly distorted 3DBL therefore demonstrates a complexity associated with all perturbed boundary layers, in that the regions away from and very near the wall are dominated by separate inner- and outer-layer dynamics (Smits & Wood 1985).

Mean three-dimensionality is most fundamentally quantified not by the mean crossflow but by the non-zero mean streamwise vorticity associated with the mean spanwise shear $\partial W/\partial y$. (The x, y, and z coordinates, with corresponding U, V, and W velocity components, are used throughout to respectively denote the streamwise, wall-normal, and spanwise directions, with respect to a two-dimensional reference flow for which W is identically zero. In other coordinate systems non-zero $\partial W/\partial y$ might simply correspond to a two-dimensional flow directed away from the x-axis, and therefore not necessarily represent a lack of orthogonality of the mean velocity and mean vorticity, as it does here.) In the course of examining the impact of mean-flow changes upon the inner and outer regions, it is useful to differentiate between two types

† The effect of mean three-dimensionality upon the near-wall turbulence structures has been studied by Sendstad & Moin (1992), Littel & Eaton (1994), Kang, Choi & Yoo (1998), Le, Coleman & Kim (1999), Kiesow & Plesniak (1999), and Le (1999).

of perturbed 3DBL found in practice, according to the manner in which mean three-dimensionality (that is, $\partial W/\partial y$) is introduced to the flow. In the first, the pressure-driven variety,† $\partial W/\partial y$ appears in the outer layer because of inviscid skewing arising from streamwise variations of the mean spanwise pressure gradient. Mean streamwise vorticity (i.e. $\partial W/\partial y$) is induced by the irrotational strain $\partial W/\partial x = \partial U/\partial z$ (such that $\Omega_y \equiv 0$) which 'scissors' (rotates in opposite directions) the mean velocity $\boldsymbol{U}$ and mean vorticity $\boldsymbol{\Omega}$ vectors in the streamwise–spanwise (x, z) plane: the initial spanwise mean vorticity $(\partial U/\partial y)$ is redirected such that it has a streamwise component $(\partial W/\partial y)$ (Bradshaw 1987); see figure 3(*a*) below. This case includes the curved-duct, blunt-obstacle, and swept-wing experiments mentioned above. The other type of perturbed 3DBL is the mean-shear-driven version, for which spanwise shear is generated in the inner layer by a step change in surface conditions. The rotating-cylinder experiments of Furuya, Nakamura & Kawachi (1966), Lohmann (1976) and Driver & Hebbar (1991) (which involve longitudinal flow along the cylinder recovering from or first encountering a rotating section) fall into this category, as do the plane spanwise-moving-wall studies of Moin *et al.* (1990), Sendstad & Moin (1992), Jung *et al.* (1992), Laadhari *et al.* (1994), Howard & Sandham (1996), Coleman *et al.* (1996*a*), Kiesow & Plesniak (1999), and Le (1999). Our interest here is in the pressure-driven case, but we will still have occasion to consider shear-driven effects. Even in pressure-driven 3DBLs, near the surface $\partial W/\partial y$ is created by a shearing force, as the no-slip boundary condition affects the accelerating spanwise flow (figure 1*b*). Consequently outer-layer strains contain both irrotational and vortical components (representing respectively the direct and indirect effect of the skewing), while those near the surface (where skewing is negligible) are essentially vortical (i.e. rotational). That both types of 3DBL experience mean spanwise shear near the wall raises the possibility that the near-wall physics of the two flows are similar – which would explain the inner-layer reduction of $-\overline{u'v'}$ mentioned above, observed in 3DBL experiments with and without a spanwise pressure gradient. Addressing this issue is another goal of this work.

A consistent trend in all perturbed 3DBLs is a reduction of the ratio of the magnitude of the Reynolds shear stress to the turbulence kinetic energy, compared to the initial equilibrium two-dimensional state. As pointed out by Schwarz & Bradshaw (1994), this alteration of the statistical structure of the flow implies that the turbulence becomes less efficient in extracting energy from the mean after $\partial W/\partial y$ has appeared, presumably as the result of the imposed strain deforming the turbulent eddies compared to the natural shape that they develop in two-dimensional flow. However, other types of outer-layer strains – notably those due to adverse pressure gradients (APGs) – are also known to diminish the stress/energy ratio (Nagano, Tagawa & Tsuji 1991; Spalart & Watmuff 1993; Coleman *et al.* 1997). Further complicating the picture is the fact that most (if not all) practical 3DBLs are subject to a combination of spanwise (inviscid skewing) and streamwise (APG) strains, so it is hard to distinguish between stress/energy ratio reductions that are caused by streamwise deceleration and those due solely to mean crossflow. Schwarz & Bradshaw addressed this challenge by designing an experiment in which the streamwise pressure gradient $\partial P/\partial x$ was minimized along the centreline of their curved wind tunnel; since they found a reduction of the stress/energy ratio in the centreline plane, it appears that mean spanwise shear (either in its near-wall form, or because of the outer-layer skewing) is sufficient to modify the turbulence structure. However, since $\partial P/\partial x$ is non-zero at spanwise locations on either side of the centreline in the Schwarz & Bradshaw flow,

† Also known as skew-induced, or Prandtl's first kind of secondary flow (Bradshaw 1987).

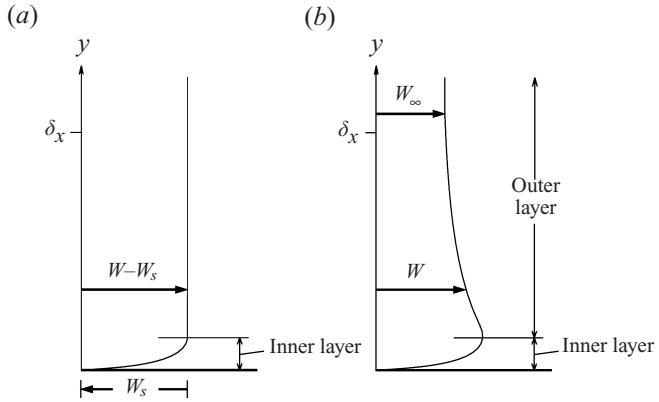

FIGURE 1. Non-stationary spanwise (lateral) mean velocity profiles in three-dimensional boundary layers. (*a*) Mean-shear-driven case: lateral flow created by surface moving with velocity W_s. (*b*) Pressure-driven case: lateral flow is an indication of non-zero $\partial W/\partial x$, which is created directly by spanwise mean pressure gradient $\partial P/\partial z$ (cf. figure 3*a*). In the outer layer spanwise shear $\partial W/\partial y$ is due to inviscid skewing of $\partial U/\partial y$; in the inner layer $\partial W/\partial y$ is caused by the no-slip condition on W. (Thickness of streamwise boundary layer denoted by δ_x.)

the possibility of the turbulence being affected by non-skewing deformations cannot be entirely ruled out. Moreover, the experimental findings of Gleyzes *et al.* (1993) and Webster, DeGraaff & Eaton (1996) (who respectively studied flows over a finite swept wing and a swept bump) suggest that pressure-driven 3DBLs may be much more sensitive to APG-induced strains (streamwise deceleration $\partial U/\partial x < 0$ and/or wall-normal divergence $\partial V/\partial y$) than to $\partial W/\partial y$. In what follows we attempt to quantify the ability of the mean skewing- and normal-strain components to separately alter the 3DBL turbulence.

Another ambiguity we hope to help resolve is that surrounding the development of the turbulent shear stresses in perturbed 3DBLs. A well-known feature of both the shear- and pressure-driven flows is the tendency for the stresses to lag behind the mean shear: the 'spanwise' component $-\overline{v'w'}$ grows very slowly (Bradshaw & Pontikos 1985; Driver & Hebbar 1987, 1991), and the spanwise-to-streamwise shear-stress ratio $\overline{v'w'}/\overline{u'v'}$ is usually much smaller than the corresponding mean velocity-gradient ratio, $(\partial W/\partial y)/(\partial U/\partial y)$. This lack of alignment between the Reynolds stress and mean shear also exists in stationary 3DBLs (see for example figure 14 of Coleman, Ferziger & Spalart 1990) but is generally largest immediately after $\partial W/\partial y$ appears in an initially stationary two-dimensional flow, as the inertia of the turbulent motions prevents them from instantly realigning with the direction of the new mean strain. The stress/strain misalignment cannot be captured by any turbulence model that assumes an isotropic (scalar) eddy viscosity, and thus represents a clear-cut inconsistency for many popular turbulence model closures. To overcome this difficulty one must understand which terms in the Reynolds-stress transport equation are responsible for slowing the growth of $-\overline{v'w'}$, and how those terms are affected by various mean deformations – two objectives that are undertaken below.

Each of the issues outlined above is addressed by employing direct numerical simulation (DNS) of a parallel-flow approximation to the 3DBL; as explained in § 2, we associate changes in time of a three-dimensional wall-bounded shear flow (3DWL, for 'three-dimensional wall layer') with convective changes of the spatially developing case of interest. Although we do not exactly recreate any existing experimental flows

using this approach, we can duplicate their defining features and connect various causes and effects in a straightforward manner. Other advantages and limitations are detailed below. The aims of this paper are to motivate and describe the numerical approach, apply it to two three-dimensional cases, and determine the general physical and modelling implications of the results, especially regarding the issues just discussed. Testing of specific turbulence models is deferred to future studies.

After introducing and formulating the strained-channel approach in the next section, the physical and numerical parameters used to obtain the DNS results are given. Two cases are simulated, one corresponding to a pressure-driven 3DBL with no APG, the other to the decelerated and skewed boundary layer over a 45° infinite swept wing. We examine the temporal evolution of the mean statistics and Reynolds-stress budgets in § 3, finding that 3DWL turbulence is much more sensitive to mean streamwise-deceleration strains than it is to the mean spanwise shear. The critical role played by the velocity–pressure-gradient terms Π_{ij} (see equation (3.2) below) in the evolution of the Reynolds-stress budgets is also documented. Finally, closing remarks are presented in § 4 regarding the broader implications of this study.

2. Approach

2.1. *Overview*

We create a perturbed 3DWL by imposing a mean strain rate and a change of the driving pressure gradient upon turbulence that had previously been in a statistically stationary state. Incompressible turbulent two-dimensional plane channel flow is subjected to spatially uniform divergence-free irrotational distortions characteristic of those induced in the outer region of turbulent boundary layers by pressure gradients. Solutions are obtained using DNS to resolve all relevant scales of motion, so no turbulence or subgrid-scale model is needed.

This strained-channel strategy is based on the observation that the pertinent characteristic of the pressure-driven boundary layer is not the pressure gradient as such, but the mean strains (such as the $\partial W/\partial x = \partial U/\partial z$ skewing, and $\partial U/\partial x = -\partial V/\partial y < 0$ deceleration) that they cause. We utilize a three-dimensional flow domain that is spatially periodic in the streamwise x and spanwise z directions and has two no-slip plane walls, and approximate the real spatially developing problem with a temporally evolving one. The channel turbulence is subjected to mean-flow variations in time that correspond to convective changes experienced by the turbulence in a boundary layer. The defining features of spatially developing pressure-driven shear layers are thereby captured in a wall-bounded flow that maintains its streamwise and spanwise homogeneity. When averages are discussed we use $\boldsymbol{U}$ and $\overline{\boldsymbol{u}}$ respectively to denote the imposed deformations, and the temporally evolving profiles in the channel (sampling over the directions parallel to the walls, and referring velocities to the local wall value). The streamwise/spanwise homogeneity is the reason explicit strains must be added to emulate the pressure-driven flow. Merely applying a spanwise pressure gradient (which is uniform in space by definition) in the channel results in a purely shear-driven 3DWL (cf. Moin *et al.* 1990) – since the effect of a spatially uniform pressure gradient in one direction is equivalent to an acceleration of the channel walls in the other (Sendstad & Moin 1992). (The distinction between previous and present three-dimensional channel flows is thus illustrated in figure 1: the shear-driven case (figure 1*a*) corresponds to the spanwise pressure-gradient/moving-wall DNS of Moin *et al.* (1990) and Coleman *et al.* (1996*a*), the pressure-driven case (figure 1*b*) to

the present simulations.) A primary test of the correctness of this approach will be verification that the outer-layer mean velocity profiles evolve according to the Squire–Winter–Hawthorne (SWH) criterion in the appropriate limits† (Squire & Winter 1951; Hawthorne 1951, 1954; Bradshaw 1987).

The imposed strain field is given by the divergence-free irrotational deformation,

$$\mathscr{A}_{ij} \equiv \frac{\partial U_i}{\partial x_j} = \begin{bmatrix} \partial U/\partial x & 0 & \partial U/\partial z \\ 0 & \partial V/\partial y & 0 \\ \partial W/\partial x & 0 & \partial W/\partial z \end{bmatrix}, \tag{2.1a}$$

where

$$\mathscr{A}_{ii} = \mathscr{A}_{11} + \mathscr{A}_{22} + \mathscr{A}_{33} = 0, \quad \text{and} \quad \mathscr{A}_{13} = \mathscr{A}_{31}. \tag{2.1b,c}$$

This form is chosen so that the y (wall-normal) direction is a principal axis of the strain tensor (hence the four zeros in (2.1a)). Because of the irrotationality constraint (2.1c) the imposed mean strain $\mathscr{S}_{ij} = \frac{1}{2}(\mathscr{A}_{ij} + \mathscr{A}_{ji})$ is equivalent to $\mathscr{A}_{ij}$. Each component $\mathscr{A}_{ij}$ is assumed to be a function of time only, and therefore uniform in space. Spatial uniformity of $\mathscr{A}_{ij}$ in the streamwise and spanwise directions is consistent with homogeneity. The lack of y dependence maintains a rectangular domain, as required by the code. We use only simple time histories here, in which the strain is off until time zero and constant from then on. (A broader range of perturbed flows could also be considered simply by imposing a series of distinct $\partial\,\mathscr{A}_{ij}/\partial t = 0$ phases one after the other, or by suddenly removing the constant strain and examining the return toward the fully developed two-dimensional state. When less-sudden perturbations are desired, the strain rate could be gradually applied, with for example $\mathscr{A}_{ij}$ increasing smoothly from zero at $t = 0$ to an asymptotic value at finite time.) The strain supplies a continuous source of momentum and energy to the flow, as well as a redistribution of energy between components (see equations (2.7a), (2.10a) and (3.3b) below).

There are three independent strain parameters in (2.1a). The rates of stretching or compression in the wall-normal direction y and in two mutually orthogonal directions in the (x, z)-plane all sum to zero, thus defining the first two parameters. The third is the orientation (defined by the 'angle of sweep' – so termed for reasons given in the next section) of the horizontal stretching/compression axis with respect to x, the direction of the initial two-dimensional flow. When this angle is zero, the (x, z) coordinates coincide with the principal axes of the horizontal plane strain, and $\mathscr{A}_{13} = \mathscr{A}_{31} = 0$. Although these three outer quantities, which are associated with the distorting or warping influence of the mean pressure gradient, completely determine the behaviour of the flow away from the surface, there are two more parameters needed in order to fully represent the impact of pressure-gradient $\nabla\mathscr{P}$ variations. They quantify the 'bulk' effect of $\nabla\mathscr{P}$ as it accelerates/decelerates the core of the channel flow, which in turn creates a viscous internal layer at the surface that diffuses into the outer layer as the flow develops (Smits & Wood 1985; Bradshaw 1987). A description of these two inner parameters follows.

The relationship between the temporally evolving and spatial flows is quantified by defining a vector $\boldsymbol{U}_{\text{avg}} = (U_{\text{avg}}, W_{\text{avg}})$ that is representative of the mean velocity in the outer layers of both flows. The time derivative of our flow, $\partial/\partial t$, approximates the material derivative $U_{\text{avg}}\partial/\partial x + W_{\text{avg}}\partial/\partial z$ in the spatial case. We further associate the three straining parameters in (2.1a), $\mathscr{A}_{11}$, $\mathscr{A}_{33}$, and $\mathscr{A}_{13} = \mathscr{A}_{31}$, with the strains imposed in the free stream of the 3DBL, $\partial U_\infty/\partial x$, $\partial W_\infty/\partial z$, and $\partial U_\infty/\partial z = \partial W_\infty/\partial x$,

† The agreement cannot be exact, since only inviscid terms enter the SWH prediction.

respectively. We assume that the strain rates in the outer layer of the 3DBL are close to those in the free stream, which is justified by their relatively large magnitude (compared to the outer-layer shear, or equivalently the timescale of the large eddies) and the small defect found in practice particularly at high Reynolds numbers; in other words $(U_{\mathrm{avg}}, W_{\mathrm{avg}}) \approx (U_\infty, W_\infty)$.

Each point of the flow volume is affected by the strain (see figures 3*c* and 14*c*). We are distorting the fluid and the computational box consisting of the periodic boundaries in x and z, and the two walls at $y = \pm\delta(t)$, where δ is the channel half-width, which when $\mathscr{A}_{22} \neq 0$ is a function of time. Physically the channel walls have become elastic impervious membranes, which remain plane and parallel and continue to enforce the no-slip condition. The fact that the walls are elastic slightly obscures the comparison between the near-wall regions of the present and actual pressure-driven boundary layers, making this study most relevant to the behaviour of the outer layer. But since typical 3DBL strains are weak compared with the shear rate near the wall (and therefore the inverse of the turbulence time scale), it is possible to draw conclusions about the near-wall layer as well.

It is helpful to differentiate between the irrotational and vortical mean fields. The former is prescribed solely by $\mathscr{A}_{ij}$, while the latter is due to wall-normal variations of the mean streamwise $\overline{u}$ and spanwise $\overline{w}$ velocity between the walls:

$$\mathscr{S}_{ij} = \begin{bmatrix} \mathscr{A}_{11} & 0 & \mathscr{A}_{13} \\ 0 & \mathscr{A}_{22} & 0 \\ \mathscr{A}_{31} & 0 & \mathscr{A}_{33} \end{bmatrix} + \begin{bmatrix} 0 & \frac{1}{2}\partial\,\overline{u}/\partial y & 0 \\ \frac{1}{2}\partial\,\overline{u}/\partial y & 0 & \frac{1}{2}\partial\,\overline{w}/\partial y \\ 0 & \frac{1}{2}\partial\,\overline{w}/\partial y & 0 \end{bmatrix}, \tag{2.2a}$$

but $\boldsymbol{\Omega} = \nabla \times (\boldsymbol{U} + \overline{\boldsymbol{u}})$ is

$$\Omega_i = \begin{pmatrix} 0 \\ 0 \\ 0 \end{pmatrix} + \begin{pmatrix} \partial\,\overline{w}/\partial y \\ 0 \\ -\partial\,\overline{u}/\partial y \end{pmatrix} = \overline{\omega}_i, \tag{2.2b}$$

where $\overline{\omega}_i = \epsilon_{ij\ell}\partial\,\overline{u}_\ell/\partial x_j$. We are free to choose the three independent components of the irrotational term in (2.2*a*) (in the sense that it is realistic to drive the flow with pressure gradients), but not the two wall-normal gradients $\partial\,\overline{u}/\partial y$ and $\partial\,\overline{w}/\partial y$ (which obey the vorticity transport equation). In the outer layer the correct vorticity history is induced by $\mathscr{A}_{ij}$, via inviscid skewing for example. However, because of the lack of y variation of the applied straining field, the inviscid-skewing mechanism and the other outer-layer strains will be active over the entire flow, all the way to the wall, where they are too weak to be relevant in practice. In order to also obtain the correct near-wall shear histories the walls are accelerated in the (x, z)-plane such that the difference between the mean streamwise and spanwise velocities at the channel centreline and the wall varies in time at the same rate that the outer-layer velocity in the spatial flow changes as it convects downstream.

The temporal/spatial analogy is completed by equating the free-stream (edge) velocity of the boundary layer with the difference between the mean centreline velocity of the channel $(\overline{u}_c, \overline{w}_c)$ and the wall velocity (u_w, w_w), and posing that that difference $\Delta\overline{\boldsymbol{u}}_c$ evolves as

$$\frac{\partial \Delta\overline{u}_c}{\partial t} = U_\infty \frac{\partial U_\infty}{\partial x} + W_\infty \frac{\partial U_\infty}{\partial z} = \Delta\overline{u}_c \mathscr{A}_{11} + \Delta\overline{w}_c \mathscr{A}_{13}, \tag{2.3a}$$

$$\frac{\partial \Delta\overline{w}_c}{\partial t} = U_\infty \frac{\partial W_\infty}{\partial x} + W_\infty \frac{\partial W_\infty}{\partial z} = \Delta\overline{u}_c \mathscr{A}_{31} + \Delta\overline{w}_c \mathscr{A}_{33}, \tag{2.3b}$$

where $\Delta\overline{\boldsymbol{u}}_c = (\Delta\overline{u}_c, \Delta\overline{w}_c)$, with $\Delta\overline{u}_c = \overline{u}_c - u_w$ and $\Delta\overline{w}_c = \overline{w}_c - w_w$. The histories of the two components of this velocity difference represent the final two (the inner or bulk acceleration/deceleration) independent perturbation parameters mentioned above. Their role is to ensure that $\boldsymbol{U}_{\rm avg} - \boldsymbol{u}_w$ changes in time in the strained channel much as it does in the downstream direction in the spatially developing flow, so that the appropriate inner layer (i.e. near-wall shear) will result. Since the mean shear near the wall is typically much greater than $\mathscr{A}_{ij}$ (whose magnitude is set by the outer-layer strain), the accelerating walls are able to duplicate gross mean-flow features of the near-wall region, such that realistic 3DWL velocity profiles are obtained over the entire channel (see figures 4 and 15 below).

The strategy outlined above allows us to systematically approximate spatial 3DBLs with a temporally evolving channel flow. Channel simulations are much more efficient than those of a spatial boundary layer, allowing a much more extensive study for a given cost. Advantages include being able to use fully developed two-dimensional channel flow as a single clearly defined initial condition, and thus to avoid the ambiguity of often-troublesome inflow and outflow conditions. Obtaining the Reynolds-stress tensor and budgets is easier from a programming point of view, and having two spatial averaging directions more than offsets the loss of homogeneity in time, when it comes to obtaining statistical samples. Spatial simulations require much larger streamwise domains, which are costly both in terms of memory and of time required to reach steady state (Spalart & Watmuff 1993; Spalart & Coleman 1997). Also, ensemble averaging can be applied over the two halves of the channel and further samples can be gathered by starting the distortion at different times of the two-dimensional simulation (Moin *et al.* 1990) or by applying it in the opposite direction. Another benefit is the generality: combinations of distortions and wall-velocity histories can be arranged to isolate pure straining effects, two-dimensional or three-dimensional, or to closely approximate deformations experienced by the near-wall and outer regions of a wide range of boundary layers. The generality of most spatial DNS studies is constrained by their homogeneity in the spanwise direction. A final advantage is that the simulation statistics depend only on time and the wall-normal coordinate y, which implies that an unsteady one-dimensional problem can be used to investigate 3DBL physics and to test and develop turbulence models for various spatially evolving flows. Reynolds-averaged solutions can be obtained rapidly from a personal computer.

2.2. *Problem formulation*

An incompressible flow with velocity $\mathscr{V}_i\,(i = 1, 2, 3)$ and pressure $\mathscr{P}$ is considered in an orthogonal reference frame $\boldsymbol{x} = (x_1, x_2, x_3) = (x, y, z)$. The approach is similar to that of Rogallo (1981) (see also Lee & Reynolds 1985), except that instead of distorting spatially homogeneous turbulence $\boldsymbol{u}'(\boldsymbol{x}, t)$, here the flow $\boldsymbol{u}(\boldsymbol{x}, t)$ is between two no-slip surfaces and will contain both fluctuations $\boldsymbol{u}'(\boldsymbol{x}, t)$ and an inhomogeneous mean $\overline{\boldsymbol{u}}(y, t)$. Rogers (2000) has also performed a homogeneous-strain/inhomogeneous-flow DNS study, for a free shear flow.

The numerical code uses coordinates $\boldsymbol{x}^* = (x_1^*, x_2^*, x_3^*) = (x^*, y^*, z^*)$ aligned with the principal axes of the deformation tensor $\mathscr{A}_{ij}$, so that

$$\mathscr{A}_{ij}^* \equiv \frac{\partial U_i^*}{\partial x_j^*} = \begin{bmatrix} \mathscr{A}_{11}^* & 0 & 0 \\ 0 & \mathscr{A}_{22}^* & 0 \\ 0 & 0 & \mathscr{A}_{33}^* \end{bmatrix}, \tag{2.4}$$

with $\mathscr{A}^*_{ii} = 0$. We have

$$x^* = x\cos\sigma - z\sin\sigma, \quad y^* = y, \quad z^* = z\cos\sigma + x\sin\sigma, \tag{2.5a}$$

where $\boldsymbol{x} = (x, y, z)$ are the 'downstream coordinates' (x is the initial streamwise direction of the two-dimensional channel flow), and equivalent relations for the velocity components. The angle σ is defined as positive when clockwise (i.e. from x toward z – see figure 3*c*). Because of its meaning over swept wings (which nominally impose a strain at a right angle to their leading edge; Bradshaw & Pontikos 1987), σ will be referred to as the angle of sweep. We have

$$\mathscr{A}_{11} = \mathscr{A}^*_{11}\cos^2\sigma + \mathscr{A}^*_{33}\sin^2\sigma, \tag{2.5b}$$

$$\mathscr{A}_{22} = \mathscr{A}^*_{22}, \tag{2.5c}$$

$$\mathscr{A}_{33} = \mathscr{A}^*_{11}\sin^2\sigma + \mathscr{A}^*_{33}\cos^2\sigma, \tag{2.5d}$$

$$\mathscr{A}_{13} = \mathscr{A}_{31} = -\mathscr{A}^*_{11}\cos\sigma\sin\sigma + \mathscr{A}^*_{33}\cos\sigma\sin\sigma. \tag{2.5e}$$

As mentioned above, there are three independent strain parameters: σ and any two of $\mathscr{A}^*_{11}$, $\mathscr{A}^*_{22}$ and $\mathscr{A}^*_{33}$, with the third following from $\mathscr{A}^*_{ii} = 0$. With respect to the downstream axes, the independent parameters are $\mathscr{A}_{13}$ and any two of $\mathscr{A}_{11}$, $\mathscr{A}_{22}$ and $\mathscr{A}_{33}$.

The straining is imposed for $t \geqslant 0$ and the initial condition at $t = 0$ is fully developed turbulent plane channel flow. At $t = 0$ the flow becomes

$$\mathscr{V}_i(\boldsymbol{x}, t) = u_i(\boldsymbol{x}, t) + U_i(\boldsymbol{x}, t), \tag{2.6}$$

and the pressure $\mathscr{P}$ changes from p to $p + \mathscr{Q}$. The imposed deformation field U_i varies linearly in space according to $U_i(\boldsymbol{x}, t) = \mathscr{A}_{ij}(t)\, x_j$, where the spatially uniform velocity gradient $\mathscr{A}_{ij}$ is given by (2.1), and each component is a function solely of time.

The DNS domain is aligned with the principal axes of the superimposed strain, with the walls at $y^* = y = \pm\delta$. When $\sigma \neq 0$ a 'swept' initial condition is used; that is the initial two-dimensional flow direction is oriented at the angle σ with respect to the x^*-axis (cf. figure 3*c* below), by specifying that the z^*-component of the bulk mass flux be non-zero. (The initial conditions are obtained by running the strained-channel code with no strain, as a conventional Poiseuille DNS.) Each component of $\boldsymbol{u}^*$ is required to satisfy the no-slip condition $\boldsymbol{u}^* = \boldsymbol{u}^*_w$ at $y = \pm\delta$, where $\boldsymbol{u}^*_w = (u^*_w, 0, w^*_w)$ is the velocity of the walls.

As a result of (2.6), the 'embedded' wall-bounded flow $\boldsymbol{u}^*$ will be strained at the rate $\mathscr{S}^*_{ij} = \frac{1}{2}(\mathscr{A}^*_{ij} + \mathscr{A}^*_{ji}) = \mathscr{A}^*_{ij}$, and will satisfy

$$\frac{\partial u^*_i}{\partial t} + u^*_j\mathscr{A}^*_{ij} + u^*_j\frac{\partial u^*_i}{\partial x^*_j} = -\left.\frac{\partial \overline{p}}{\partial x^*_i}\right|_{\text{app}} - \frac{\partial p'}{\partial x^*_i} + \frac{1}{Re}\frac{\partial^2 u^*_i}{\partial x^*_j\partial x^*_j} - \mathscr{A}^*_{j\ell}x^*_\ell\frac{\partial u^*_i}{\partial x^*_j} \tag{2.7a}$$

and

$$\frac{\partial u^*_i}{\partial x^*_i} = 0. \tag{2.7b}$$

All variables in (2.7) are non-dimensionalized by the initial channel half-width $\delta(0)$ and a reference velocity U_{ref} (which here will be of the order of the initial friction velocity $u_\tau(0)$). The reference Reynolds number is $Re = U_{\text{ref}}\delta(0)/\nu$, where ν is the kinematic viscosity, and p is the non-dimensional kinematic pressure, which we have decomposed into its mean $\overline{p}$ and fluctuating component p'. The quantity $\partial\overline{p}/\partial x^*_i\big|_{\text{app}}$ is the applied mean pressure gradient, a time-dependent, spatially uniform body force.

The momentum contribution for the imposed field was removed from (2.7*a*) because it is curl-free:

$$\left(\frac{\partial U_i^*}{\partial t} + U_\ell^* \mathscr{A}_{i\ell}^*\right) = \left(\frac{\partial \mathscr{A}_{ij}^*}{\partial t} + \mathscr{A}_{i\ell}^* \mathscr{A}_{\ell j}^*\right) x_j^* = -\frac{\partial \mathscr{Q}}{\partial x_i^*}, \tag{2.8}$$

and is attributed to a pressure field $\mathscr{Q}$, which is quadratic in space.

Following Rogallo (1981) we now introduce the coordinates

$$\xi_i = \mathscr{B}_{ij}(t)\, x_j^*, \quad \widehat{t} = t, \tag{2.9a}$$

defined by the transformation $\mathscr{B}_{ij}$, subject to the constraint that the new spatial variables (ξ_1, ξ_2, ξ_3) be material properties of the imposed strain flow:

$$\frac{\partial \xi_i}{\partial t} + U_j \frac{\partial \xi_i}{\partial x_j^*} = \left(\frac{\partial \mathscr{B}_{ij}}{\partial t} + \mathscr{B}_{i\ell} \mathscr{A}_{\ell j}^*\right) x_j^* = 0,$$

or

$$\frac{\partial \mathscr{B}_{ij}}{\partial t} + \mathscr{B}_{i\ell} \mathscr{A}_{\ell j}^* = 0, \tag{2.9b}$$

and $\mathscr{B}_{ij}(0) = \delta_{ij}$. This choice for (2.9) removes the secular term (explicitly containing x_i^*) from (2.7*a*) and thus allows periodic conditions in planes parallel to the walls. The distance (measured in x_i^*) between lines of constant ξ_i indicates the total amount of deformation produced by $\mathscr{A}_{ij}^*$. Transforming (2.7) from (x_i^*, t) to $(\xi_i, \widehat{t})$ coordinates, and using (2.9*b*), gives

$$\frac{\partial u_i^*}{\partial \widehat{t}} + u_j^* \mathscr{A}_{ij}^* + u_j^* \mathscr{B}_{\ell j} \frac{\partial u_i^*}{\partial \xi_\ell} = -\left.\frac{\partial \overline{p}}{\partial x_i^*}\right|_{\text{app}} - \mathscr{B}_{\ell i} \frac{\partial p'}{\partial \xi_\ell} + \frac{1}{Re} \mathscr{B}_{\ell j} \mathscr{B}_{nj} \frac{\partial^2 u_i^*}{\partial \xi_\ell \partial \xi_n} \tag{2.10a}$$

and

$$\mathscr{B}_{ji} \frac{\partial u_i^*}{\partial \xi_j} = 0, \tag{2.10b}$$

which are subject to the boundary conditions $\boldsymbol{u}^* = \boldsymbol{u}_w^*$ at $\xi_2 = \pm 1$. The form of (2.10) is identical to that for simple Poiseuille flow, except for the time-dependent metric terms $\mathscr{B}_{ij}$ multiplying each spatial derivative, and the $\mathscr{A}_{ij}^*$ term on the left-hand side. It is, however, important to bear in mind the new significance of the unsteady term in (2.10*a*), which now indicates the temporal change at fixed $\xi_i(\boldsymbol{x}^*, t) = \mathscr{B}_{ij}(t)\, \xi_j(\boldsymbol{x}^*, 0)$ (rather than at fixed x_i^*). For modelling studies, the Reynolds-averaged equations can be deduced from (2.10*a*).

To solve (2.10) a closed-form expression for the coordinate-mapping function $\mathscr{B}_{ij}(t)$ is required. Limiting our attention to the special case of constant strain rate, for which $\partial \mathscr{A}_{ij}^*/\partial t = 0$, we have for the solution of (2.9*b*)

$$\mathscr{B}_{ij}(t) = \begin{bmatrix} \exp(-\mathscr{A}_{11}^* t) & 0 & 0 \\ 0 & \exp(-\mathscr{A}_{22}^* t) & 0 \\ 0 & 0 & \exp(-\mathscr{A}_{33}^* t) \end{bmatrix}. \tag{2.11}$$

Applying (2.11) to (2.9*a*) reveals the histories of the channel half-width,

$$\delta(t) = \delta(0) \exp(\mathscr{A}_{22}^* t), \tag{2.12a}$$

and of the horizontal domain sizes Λ_{x^*} and Λ_{z^*} in the x^*- and z^*-directions,

$$\Lambda_{x^*}(t) = \Lambda_{x^*}(0) \exp(\mathscr{A}_{11}^* t) \quad \text{and} \quad \Lambda_{z^*}(t) = \Lambda_{z^*}(0) \exp(\mathscr{A}_{33}^* t). \tag{2.12b,c}$$

Equation (2.12) shows how the DNS domain deforms when $\mathscr{A}_{ij}^*$ is constant in t. (Recall that other straining histories are possible.)

We now consider the wall-velocity histories $\boldsymbol{u}_w^*(t)$ needed to control the temporal evolution of the rotational mean-velocity gradients near the walls. As explained above, this is done by ensuring that the centreline–wall mean velocity difference $\Delta\overline{\boldsymbol{u}}_c^*$ satisfies equation (2.3), which in principal-strain axes reduces to

$$\frac{\partial \Delta\overline{u}_c^*}{\partial t} = \Delta\overline{u}_c^* \mathscr{A}_{11}^*, \tag{2.13a}$$

$$\frac{\partial \Delta\overline{w}_c^*}{\partial t} = \Delta\overline{w}_c^* \mathscr{A}_{33}^*, \tag{2.13b}$$

with $\Delta\overline{u}_c^* = \overline{u}_c^* - u_w^*$ and $\Delta\overline{w}_c^* = \overline{w}_c^* - w_w^*$. The simplest way to enforce (2.13)– the approach used to generate the results presented below – is to monitor the mean centreline velocity and adjust $\boldsymbol{u}_w^*$ according to

$$u_w^*(t) = \overline{u}_c^*(t) - \overline{u}_c^*(0)\exp(\mathscr{A}_{11}^* t), \tag{2.14a}$$

$$w_w^*(t) = \overline{w}_c^*(t) - \overline{w}_c^*(0)\exp(\mathscr{A}_{33}^* t), \tag{2.14b}$$

where $\overline{u}_c^*(0)$ and $\overline{w}_c^*(0)$ are the initial mean centreline velocities, the values at the instant the strain is imposed. We notice that the wall velocities explicitly depend on $\mathscr{A}_{ij}$ and t through the exponential terms in (2.14). (They are also affected by the influence of $\mathscr{A}_{ij}$ on $\overline{\boldsymbol{u}}_c$.) During the computation the centreline values from the previous timestep are used to prescribe the wall velocities needed to calculate the current step.

More-empirical approaches can also be taken to specify u_w^* and w_w^*. The one used for our earlier finite-$\mathscr{A}_{13}$ DNS results (Coleman *et al.* 1996*b*, 1997) was based on closing the inner leg of the mean velocity hodograph. While this more *ad hoc* method successfully causes the mean spanwise velocity profile $\overline{w}(y)$ to develop in time as it should (see figure 2 of Coleman *et al.* 1997), control of the streamwise component $\overline{u}$ is less satisfactory, especially when normal-strain components are applied, which prompted us to employ the simpler and more rigorous formulation (2.14) for the present simulations. As we shall see below, since it yields centreline–wall velocity histories in close agreement with both (2.13*a*) and (2.13*b*), equation (2.14) produces streamwise and spanwise velocities that both evolve as the spatial–temporal analogy requires.

To complete the problem formulation we describe the behaviour of the pressure gradients $\nabla^*\overline{p}\,|_{\mathrm{app}} = (\partial\overline{p}/\partial x^*, 0, \partial\overline{p}/\partial z^*)_{\mathrm{app}}$ that appear on the right-hand sides of (2.7*a*) and (2.10*a*). Before the $\mathscr{A}_{ij}^*$ strain is applied, they balance the mean wall-shear stress in the average. They can be constant in time (allowing temporal fluctuations of centreline velocity and total mass flux), or dynamically adjusted to keep the mean centreline velocity constant (which would be most consistent with our approach during the strain), or dynamically adjusted to keep the total mass flux constant. We use the third procedure, since it causes the two-dimensional statistics to converge more rapidly (Kim, Moin & Moser 1987). In the limit of an infinitely large domain (for which fully converged statistics would result from a single plane average) the three approaches would give identical results. Because the governing equations are invariant under streamwise and spanwise accelerations, whether we use $\nabla^*\overline{p}\,|_{\mathrm{app}}$ or $\boldsymbol{u}_w^*$ to control the velocity difference between the outer layer and the channel walls is irrelevant. Once the strain is applied, we specify $\Delta\overline{u}_c^*$ via (2.14), and set and maintain $\nabla^*\overline{p}\,|_{\mathrm{app}}$ equal to zero.

Case	$\mathscr{A}_{13}\delta(0)/u_\tau(0)$	$\mathscr{A}_{11}\delta(0)/u_\tau(0)$	$\mathscr{A}_{22}\delta(0)/u_\tau(0)$	$\mathscr{A}_{33}\delta(0)/u_\tau(0)$
S45	0.735	0	0	0
AS45	0.735	−0.735	+1.47	−0.735

TABLE 1. Parameters for the two straining cases.

$\Lambda_{x^*}/\delta(0)$	$\Lambda_{z^*}/\delta(0)$	m_{x^*}	m_{y^*}	m_{z^*}	n_{x^*}	n_{y^*}	n_{z^*}
$8\pi/3$	$8\pi/3$	256	129	256	384	129	384

TABLE 2. Numerical parameters.

Solutions to (2.10) are obtained using a modified version of the spectral channel code of Kim *et al.* (1987). It expresses dependent variables as Fourier series in ξ_1 and ξ_3, and via Chebychev polynomials in ξ_2. No-slip conditions are enforced using the tau method (Lanczos 1956), and a mixed Crank–Nicolson/Runge–Kutta time-advance scheme is employed (Spalart, Moser & Rogers 1991). Further details of the solution procedure are given in the Appendix.

2.3. *Cases*

Two straining fields are considered here, defined by the components summarized in table 1. Both cases correspond to 3DBLs, in that the angle of sweep σ and therefore the skewing $\mathscr{A}_{13} = \mathscr{A}_{31}$ are non-zero. We choose $\sigma = 45^\circ$ and set $\mathscr{A}_{13}$ to $0.735\ u_\tau(0)/\delta(0)$, the initial wall-friction-velocity to channel-half-width ratio. The rationale for these choices is given below. For now we note that the first case, denoted S45 ('S' to indicate non-zero skewing, '45' the angle of sweep), has no normal components, and thus supplies the effect of a mean crossflow with no streamwise pressure gradient (PG); the second strain, Case AS45, combines skewing with streamwise deceleration and wall-normal stretching to create the deformation imposed by an idealized 45°-swept wing (hence the notation AS45 – 'A' for adverse-pressure-gradient, 'S45' for $\sigma = 45^\circ$ skewing).

The numerical parameters used for both cases are listed in table 2, where Λ_{x^*} and Λ_{z^*} are the horizontal domain sizes in the principal-strain coordinates, and $(m_{x^*}, m_{y^*}, m_{z^*})$ and $(n_{x^*}, n_{y^*}, n_{z^*})$ are respectively the number of expansion coefficients and collocation (quadrature) points in the x^*-, y^*-, and z^*-directions. Even though the initial Reynolds number for these runs is the same as that used by Kim *et al.* (1987) for their two-dimensional study, $Re_\tau = u_\tau\delta/\nu \approx 180$, the three-dimensional nature of the present flows requires a larger computational expense (i.e. a square horizontal domain), due to the non-zero angle of sweep and the crossflow development. Aliasing (quadrature) errors are minimized by setting $n_{x^*} = 3m_{x^*}/2$ and $n_{z^*} = 3m_{z^*}/2$. (Total aliasing-error control is not possible, since assigning $n_y^* = 3m_y^*/2$ would compromise the no-slip boundary conditions.) Spectra and two-point correlations from Case AS45 at $\mathscr{A}_{13}t = 0.125$ are shown in figure 2, from locations near the wall and the centreline; Case S45 results are similar. The effect of the deformation, which for this case involves a compression in the x^*- direction, can be seen in the spectra by the shift of energy to higher wavenumbers, compared to the initial distribution. In the correlations the influence of $\mathscr{A}_{11}^* < 0$ is apparent from the reduction of the length of maximum streamwise separation (a measure of the largest structures that can be faithfully represented within the domain) from $0.5\Lambda_x^*(0)$ at $t = 0$ to about $0.39\Lambda_x^*$ at the time shown. Despite the strain-induced change of scale of the turbulence, the spectra and

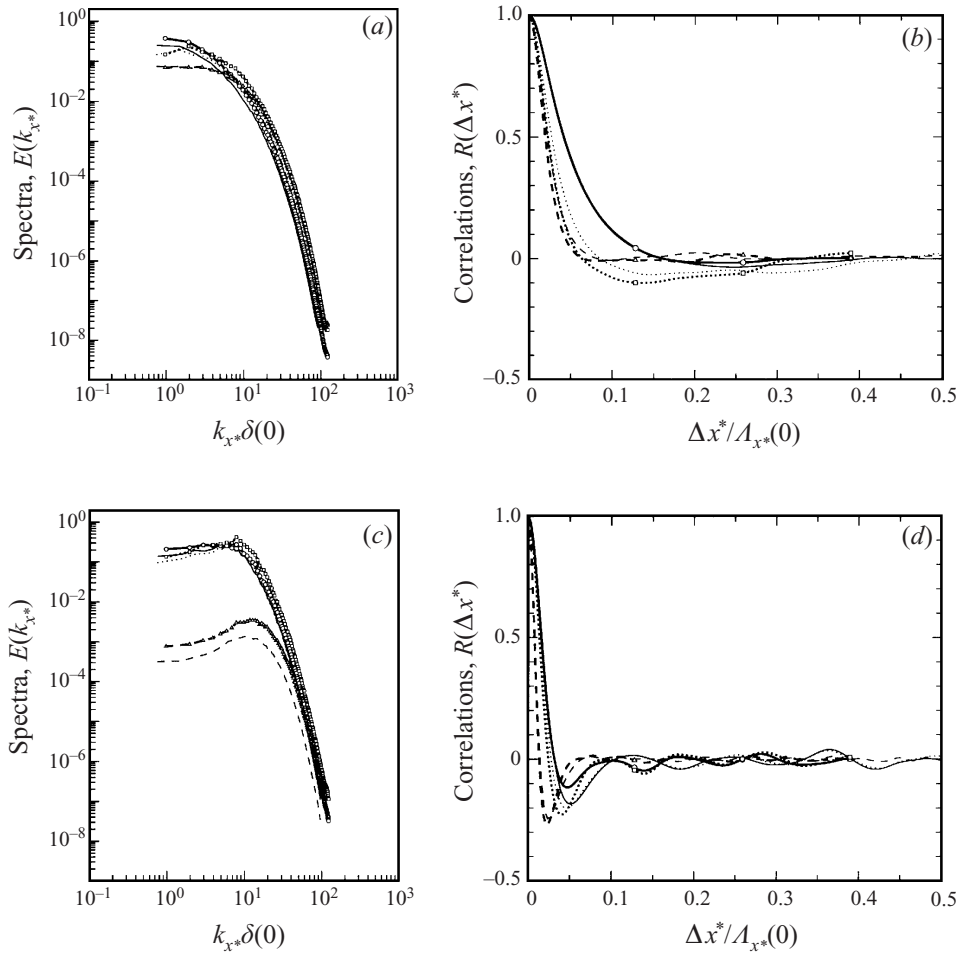

FIGURE 2. One-dimensional Fourier spectra and two-point correlations in principal-strain direction x^* for Case AS45: ——, u^* component; - - - -, v^*; ·····, w^*. Curves with and without symbols respectively denote $\mathscr{A}_{13}t = 0.125$ results and unstrained initial conditions at $\mathscr{A}_{13}t = 0$. (a,b) near centreline, $y_w/\delta(0) = 0.805$; (c,d) near walls, $y_w/\delta(0) = 0.03$.

correlations reveal that the resolution and domain size are sufficient to capture both the smallest and largest spatial structures.

Multiple Case S45 and AS45 simulations were performed using the same strain parameters for statistically independent realizations of the two-dimensional Poiseuille initial conditions. These $\sigma = 45°$ initial conditions were obtained by specifying that the bulk flow rates in x^* and z^* be equal and running the strained-channel code with no applied strain and the numerical parameters listed in table 2, until the statistics of the two-dimensional flow indicated a mature stationary state. At this point Case S45 and AS45 realizations were begun while the unstrained computation was continued until another statistically independent field for another pair of realizations was produced. The statistics presented below (denoted by an overbar) were gathered by averaging over planes parallel to the walls, over both halves of the channel, and over seven independent runs of each case.

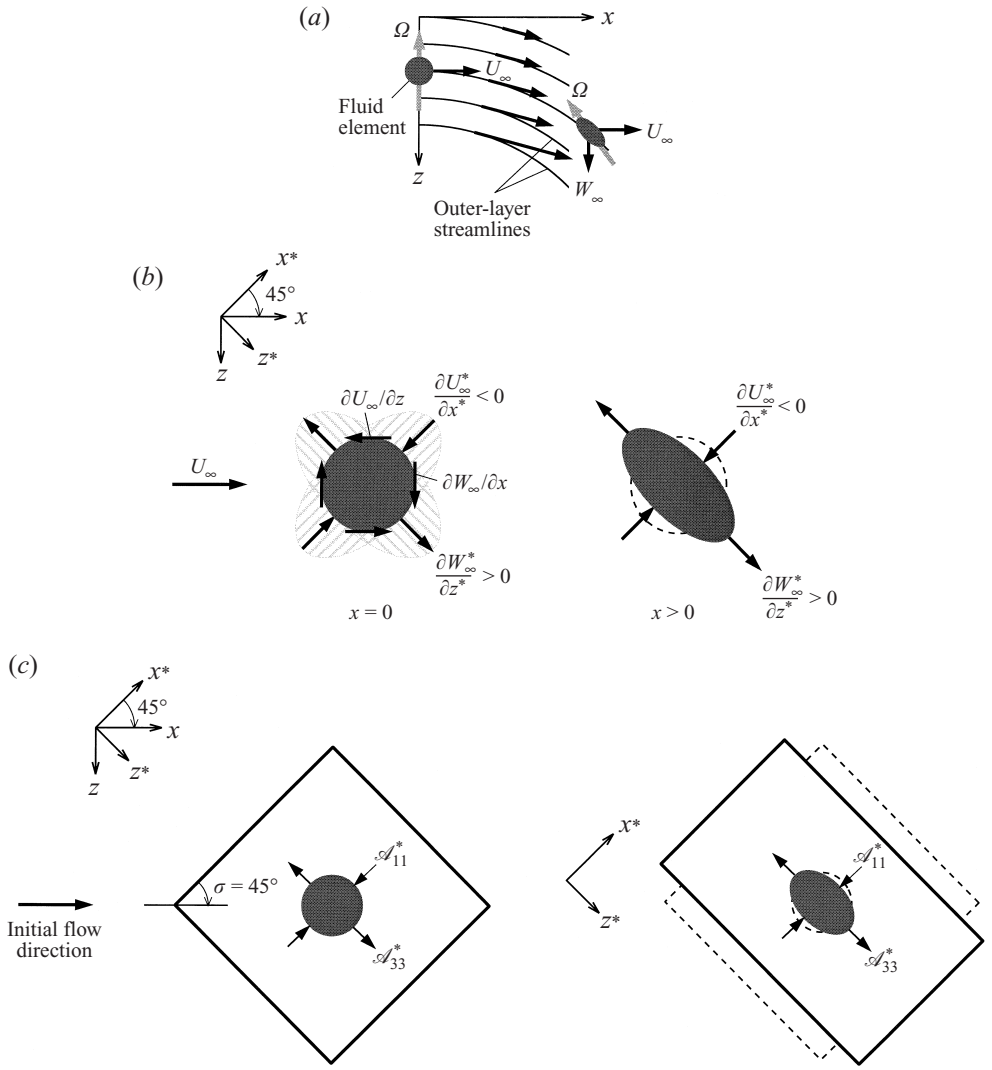

FIGURE 3. Plan view of three-dimensional wall layer subjected to pure-skewing strain. (*a*) Spatially developing flow. Outer-layer streamlines and isobars very nearly coincide. (*b*) Strain applied to fluid element of spatially developing flow and strained-channel DNS. (Cross-hatched regions represent angular distribution of normal strains.) (*c*) Initial and deformed domain of strained-channel DNS for Case S45.

3. Results

3.1. *Pure-skewing strain: Case S45*

In order to determine the influence of pure three-dimensionality unaccompanied by the complications of streamwise pressure gradients, we set $\mathscr{A}^*_{22} = 0$, $\mathscr{A}^*_{11} = -\mathscr{A}^*_{33} \neq 0$, and choose an angle of sweep $\sigma = 45°$. With respect to the initial flow direction, the resulting strain field has only $\mathscr{A}_{13} = \mathscr{A}_{31}$ as non-zero components, so that it corresponds to an idealized mean pressure gradient that always acts at a right angle to the mean flow direction (figure 3). The channel turbulence thus experiences a deformation like that imposed along the centreline of Schwarz & Bradshaw's (1994)

curved wind tunnel. Unlike the curved-duct flow, for which the streamwise gradient $\partial P/\partial x$ can only be zero at one spanwise location, here the strain field is the same at every (x, z) point in the domain. (In the Schwarz & Bradshaw duct, along trajectories outside the centreline, the streamwise gradient through the bend is first adverse then favourable, and vice versa for paths closer to the centre of curvature; see their figure 2.) Another difference between the Schwarz & Bradshaw and present flows is in the magnitude of the skewing rate. The one used here, $\mathscr{A}_{13} = 0.735u_\tau(0)/\delta(0)$, is roughly twice as large, in terms of inflow u_τ and boundary-layer thickness, as the $\partial W/\partial x$ imposed in the curved-duct experiment. For these reasons (and also because of differences in Reynolds number, and downstream variation of the rate of skewing) we cannot expect the Schwarz & Bradshaw and Case S45 statistics to correspond. Nevertheless, the flows do share enough features that their comparative behaviour should be instructive.

3.1.1. *Mean profiles and histories*

The response of the mean velocity to the applied strain and in-plane wall motion (2.14) is illustrated in figure 4. These results validate the strained-channel methodology. A key characteristic of pressure-driven three-dimensional boundary layers can be seen, namely the sudden appearance of spanwise shear $\partial\overline{w}/\partial y$ (mean streamwise vorticity) in the outer layer, due to the $\mathscr{A}_{13}$-induced skewing of the mean spanwise vorticity. The straining of the flow structures, away from their natural shapes in the two-dimensional flow, is also reproduced (although the same mean-flow behaviour could be obtained simply by injecting streamwise vorticity with a y-dependent body force, such an injection is unrealistic; the straining is required to correctly deform the outer-layer structures). The absence of streamwise acceleration (i.e. $\mathscr{A}_{11} = \mathscr{A}_{22} = 0$) causes the 'thickness' of the flow to remain constant, such that the distance δ between the wall and centreline in figure 4(*a*) is the same at all times (cf. figure 15 below). The inviscid skewing mechanism is thus the only mean-straining effect present in the outer layer. As a consequence, the $\partial\overline{w}/\partial y$ variation above the location of maximum $\overline{w}$ is inherited from the streamwise shear $\partial\overline{u}/\partial y$ of the initial flow. This explains the good agreement shown in figure 4(*b*) of the outer-layer hodograph with the straight solid lines, whose slopes are set by the Squire–Winter–Hawthorne (SWH) relationship, which assumes the mean velocity is governed solely by the effect of the skewing on the mean vorticity (Bradshaw 1987). For the present flow, using α to denote the angle through which the effective outer-layer mean velocity has turned due to the A_{13} skewing, such that $\alpha = \arctan(\mathscr{A}_{13}t)$, the SWH prediction gives $u^\perp = u^\parallel \tan(2\alpha)$, where $u^\perp$ and $u^\parallel$ are respectively the velocity components orthogonal and parallel to the current effective flow direction of the applied irrotational mean. The requirement that the mean velocity vector $(\overline{u}, \overline{w})$ change direction across a 3DWL is manifested by the finite curvature of the hodograph, as it describes the velocity distribution across both inner and outer layers. If inviscid skewing were to control the crossflow over the entire layer, and there were no near-wall shear-driven effects, the hodograph would be completely straight, and everywhere (including the origin) have the negative slope given by the SWH angle 2α. The result would be a collateral, rather than three-dimensional, flow.

The inner-layer scaling of the mean-velocity magnitude is shown in figure 4(*c*) (the symbols are from Kim *et al.*'s 1987 simulation). Noticeable departures from the initial two-dimensional profile, and from the standard law of the wall, are found as a result of the skewing. The internal boundary layer associated with the rising magnitude of

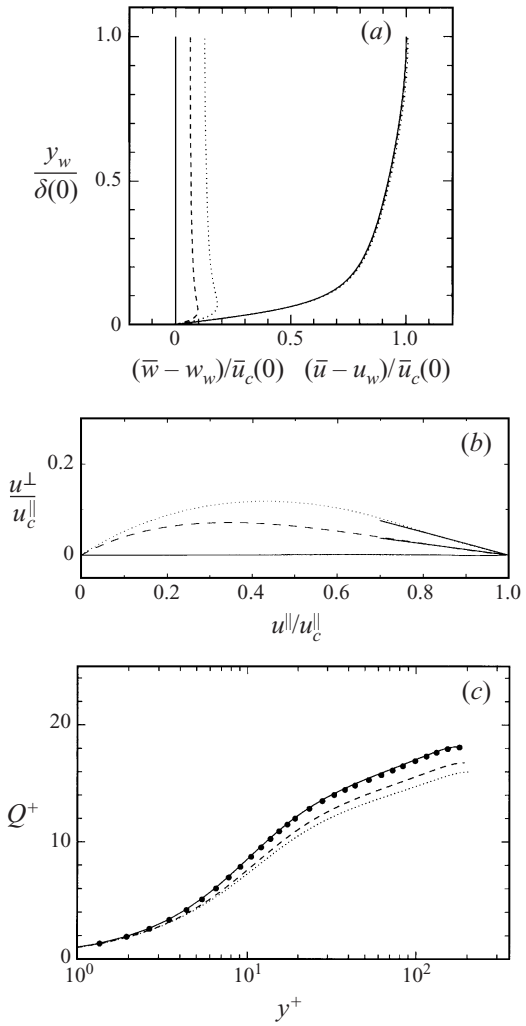

FIGURE 4. Mean velocity evolution for Case S45: ——, $\mathscr{A}_{13}t = 0$ ($\alpha = 0°$); - - - -, $\mathscr{A}_{13}t = 0.0625$ ($\alpha = 3.6°$); ·····, $\mathscr{A}_{13}t = 0.125$ ($\alpha = 7°$). (*a*) Axes aligned with initial mean flow. (*b*) Hodograph, showing components (after wall velocities removed) parallel $u^\parallel$ and normal $u^\perp$ to instantaneous coordinates aligned with current direction of mean skewing (i.e. rotated away from principal-strain coordinates (x^*, z^*) by angle $\sigma + \alpha$), normalized by parallel component at centreline $u^\parallel_c$; solid line segments denote SWH prediction. (*c*) Current wall-unit scaling; non-dimensional magnitude $Q^+ \equiv ((\overline{u}-u_w)^2 + (\overline{w}-u_w)^2)^{1/2}/u_\tau(t)$ and wall-normal coordinate $y^+ = y_w(0)\,\exp(\mathscr{A}_{22}t)\,u_\tau(t)/\nu$, where $u_\tau^2(t) = \nu[(\partial\overline{u}/\partial y)_w^2 + (\partial\overline{w}/\partial y)_w^2]^{1/2}$ is the current total wall-shear stress. Solid symbols are from two-dimensional $Re_\tau = 180$ channel of Kim *et al.* (1987).

the spanwise wall-shear stress has not propagated much higher than $y^+ \approx 10$ (cf. figures 4*a* and 4*c*).

The histories of the centreline–wall velocity differences $(\Delta\overline{u}_c, \Delta\overline{w}_c)$ responsible for the development of the inner layer are plotted in figure 5(*a*). The vertical lines in figure 5 indicate the times for which profiles are shown in other figures. These times, $\mathscr{A}_{13}t = 0$, 0.0625, and 0.125, respectively correspond to skewing angles of $\alpha = 0°$, 3.6°, and 7°. The streamwise $\Delta\overline{u}_c$ and spanwise $\Delta\overline{w}_c$ components of the centreline–wall velocity difference are given by equation (2.14), which for the Case S45 strain field

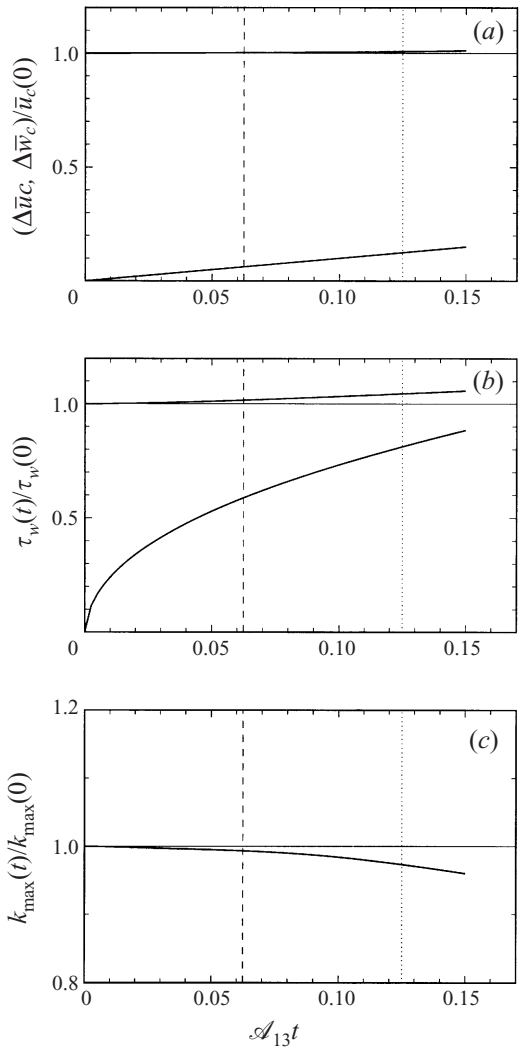

FIGURE 5. Histories of (*a*) mean centreline–wall velocity difference (equation (3.1)), (*b*) surface shear stress and (*c*) maximum turbulence kinetic energy for Case S45: upper curves, streamwise components ($\Delta\overline{u}_c = \overline{u}_c - u_w$ in (*a*), $(\tau_w)_x = \nu(\partial\,\overline{u}/\partial y)_w$ in (*b*)); lower curves, spanwise component ($\Delta\overline{w}_c = \overline{w}_c - w_w$ and $(\tau_w)_z = \nu(\partial\,\overline{w}/\partial y)_w$). Solid curve in (*c*) indicates maximum over all y_w locations of $k = \frac{1}{2}\overline{u_i' u_i'}$; (cf. figure 6*b*) (note expanded vertical scale). Vertical lines mark times for which mean profiles are shown in other figures.

are respectively

$$\frac{\overline{u}_c(t) - u_w(t)}{\overline{u}_c(0)} = \cosh(-\mathscr{A}_{13}t), \tag{3.1a}$$

$$\frac{\overline{w}_c(t) - w_w(t)}{\overline{u}_c(0)} = \sinh(-\mathscr{A}_{13}t). \tag{3.1b}$$

These dictate the evolution of the $y_w = \delta$ values of the figure 4(*a*) mean velocity profiles. The in-plane wall-velocity treatment (2.14) therefore closely approaches the desired nominally zero effective streamwise pressure gradient: (3.1*a*) yields ($\overline{u}_c -$

$u_w)/\overline{u}_c(0) = 1.006$ and 1.022 respectively at $\mathscr{A}_{13}t = 0.0625$ and 0.125. The spanwise-component history (3.1*b*) produces nearly linear growth of the effective crossflow at the centreline for the times considered (figures 4*a* and 5*a*), and ensures that the hodograph is correctly closed at the surface (figure 4*b*). This in turn develops the appropriate mean shear near the wall. Another measure of the rotational mean-flow development is shown in figure 5(*b*), where the upper curve traces the history of the streamwise mean skin friction, and the lower curve reveals the growth of the spanwise component, which is rapid. In contrast to $\Delta\overline{u}_c$ and $\Delta\overline{w}_c$, which are functions only of $\mathscr{A}_{13}t$, the drag is affected by both the external forcing (applied strain) and the turbulence. In the Schwarz & Bradshaw experiment the total skin-friction coefficient C_f was observed to remain nearly constant through the bend, instead of increasing as in figure 5(*b*). However, since before entering the bend C_f was decaying with downstream distance, the levelling off in the curved section while the boundary-layer thickness kept increasing can perhaps be viewed as a milder form of the C_f increase seen here (furthermore, their perturbation was weaker).

The upward drift in time of the streamwise component of surface shear (figure 5*b*) might suggest that the turbulence near the wall has become more vigorous as the result of the applied skewing, but the histories of the turbulent stresses reveal the opposite. A stabilizing trend is apparent in figures 6(*a*) and 6(*b*) , which respectively show a reduction with time of the profiles of streamwise Reynolds shear stress $-\overline{u'v'}$ and turbulence kinetic energy $k = \frac{1}{2}\overline{u_i'u_i'} = \frac{1}{2}q^2$. These reductions are more clearly quantified in the sub-plots in the upper-right corners of figures 6(*a*) and 6(*b*), which illustrate the amount the $\mathscr{A}_{13}t = 0.125$ profiles have changed from their initial values (the figure 6*a* inset shows the net change to $-\overline{u'v'}$; in figure 6(*b*) both k (solid symbols) and the vertical velocity variance $\overline{v'v'}$ (open symbols) are included). The decrease of k is also documented in figure 5(*c*), in terms of the history of $k_{\max}$, the largest value of k at each time. Figure 6(*b*) shows that as k decreases near the wall, the magnitude of the vertical velocity fluctuations $\overline{v'v'}$ becomes larger across the entire layer. The issue of the ultimate source of the near-wall reduction of k and inner- and outer-layer growth of $\overline{v'v'}$ will be addressed in the next subsection, where we consider the effect of the skewing on the various terms in the Reynolds-stress budgets. We shall find there that budget terms involving the pressure fluctuations play a crucial role in the evolution of the turbulence. Foreshadowing this discovery is the amplification of the pressure fluctuations themselves, whose root-mean-square values are found in figure 6(*c*).† Of particular significance is the instantaneous pressure-fluctuation increase caused by the impulsive application of the strain (compare the thin and thick solid curves,

† There is a subtlety associated with diagnosing the pressure field associated with the divergence-free velocity in the strained-channel flow: because the grid deforms in time, spatial and temporal derivatives do not commute, which introduces an extra term in the Poisson equation. The kinematic pressure p satisfies $p_{,ii} = -u^*_{j,i}u^*_{i,j} - 2u^*_{j,i}\mathscr{A}^*_{ij}$ (note the factor 2).

FIGURE 6. Profiles of (*a*) shear stress, (*b*) turbulence kinetic energy, and (*c*) root-mean-square pressure fluctuations for Case S45: ——, $\mathscr{A}_{13}t = 0$ ($\alpha = 0°$); - - - -, $\mathscr{A}_{13}t = 0.0625$ ($\alpha = 3.6°$); ·····, $\mathscr{A}_{13}t = 0.125$ ($\alpha = 7°$) (data for $\mathscr{A}_{13}t = 0.0625$ not shown in (*a*) and (*b*) to clarify presentation). Lower, middle, and upper curves in (*a*) respectively correspond to spanwise Reynolds shear stress $-\overline{v'w'}$, streamwise Reynolds shear stress $-\overline{u'v'}$, and total shear stress $(\tau)_{\text{total}} = [(\nu(\partial\,\overline{u}/\partial y) - \overline{u'v'})^2 + (\nu(\partial\,\overline{w}/\partial y) - \overline{v'w'})^2]^{1/2}$. Subplots in (*a*) and (*b*) show change with respect to initial profile (in units of background plot) of $\mathscr{A}_{13}t = 0.125$ results, of (*a*) $-\overline{u'v'}$ and (*b*) k (solid symbols), $\overline{v'v'}$ (open symbols). Thick solid (——) curve in (*c*) is $\mathscr{A}_{13}t = 0$ value immediately after strain is applied (note expanded vertical scale).

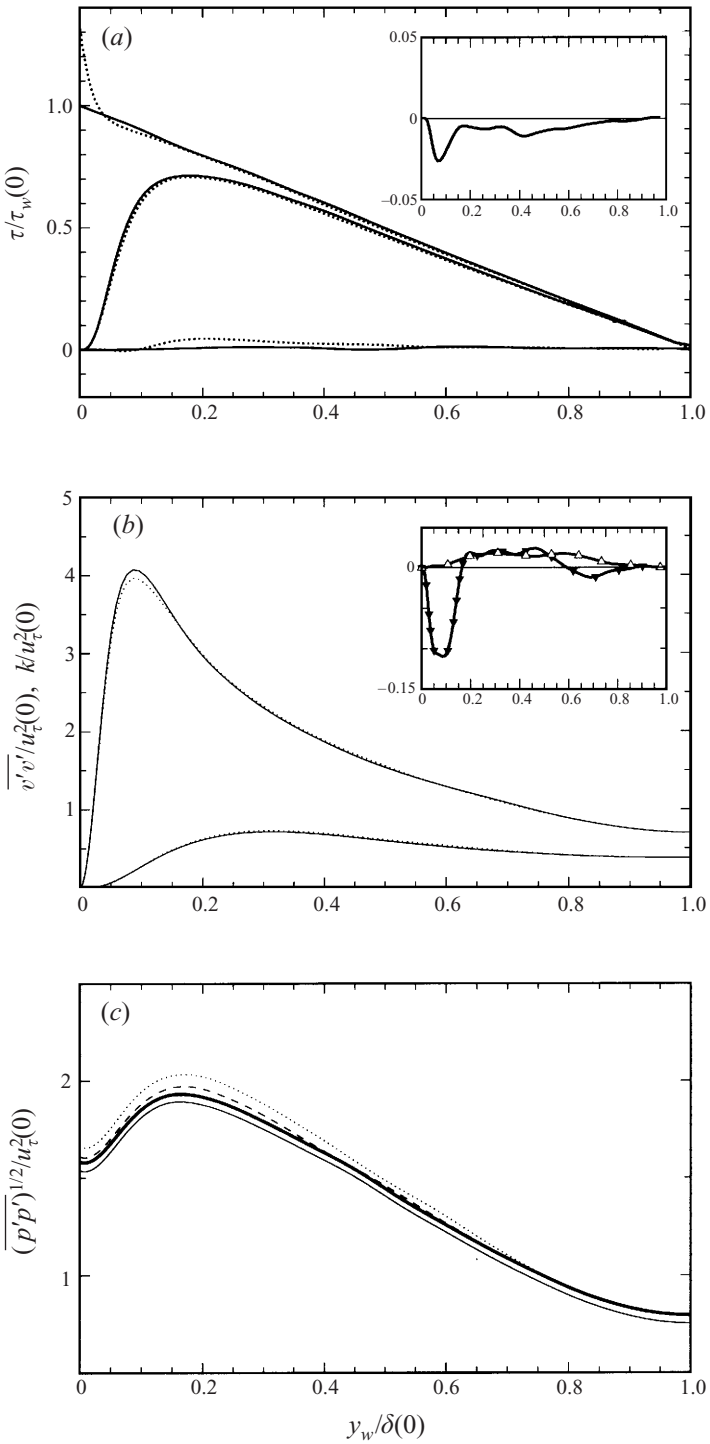

FIGURE 6. For caption see facing page.

which respectively illustrate the $\mathscr{A}_{13}t = 0$ profiles just before and just after the strain is applied). Because of the elliptic nature of an incompressible flow, the pressure–velocity correlations in the Reynolds-stress budgets exhibit step changes in time, and thus dominate the early flow history of the stresses. This will be demonstrated in § 3.1.2.

While the trend is for k and $-\overline{u'v'}$ to both decrease, the $-\overline{v'w'}$ shear stress does the opposite, with the largest growth occurring near $y_w/\delta = 0.2$ (figure 6*a*). However, although this component grows, it does so at a rate too small to immediately offset the reduction in $-\overline{u'v'}$; the magnitude $\tau = (\overline{u'v'}^2 + \overline{v'w'}^2)^{1/2}$ of the Reynolds-shear stress 'vector' $(-\overline{u'v'}, -\overline{v'w'})$ also decreases in time. The decrease is very close to that observed for the total (turbulent plus viscous) shear stress magnitude $(\tau)_{\text{total}}$ (except immediately adjacent to the wall), shown in the upper curves in figure 6(*a*). The extent to which these pure-skewing-induced changes are the result of deep structural alterations to the Reynolds-stress tensor is revealed in figure 7(*a*). This plot presents the stress/energy ratio τ/q^2 (commonly given the symbol a_1 and referred to as the Reynolds-stress structure parameter), and shows it changes very little over most of the layer, with only a slight decrease of the maximum value. The implications of stress/energy-ratio reductions, a classical feature of perturbed 3DBLs, are twofold. From a fundamental point of view it implies that the extraction of kinetic energy from the mean by the turbulence has become less efficient. From a practical point of view it indicates an inaccuracy in turbulence models that assume a_1 is constant for all flows. The reduction seen in figure 7(*a*) is not large enough to pose a grave turbulence-modelling challenge; instead it demonstrates the degree to which the stress/energy ratio is (or rather is not) modified by a pure skewing strain. We shall see when we discuss Case AS45 that when the normal strain components are also non-zero the changes in a_1 are much larger.

Another indication of the effect of the mean skewing upon the turbulence structure is given by the ratio of the turbulent flux of turbulence kinetic energy to the turbulence kinetic energy itself, $\overline{v'(u'u' + v'v' + w'w')}/(\overline{u'u' + v'v' + w'w'})$. This ratio measures the velocity V_{q^2} with which $k = \frac{1}{2}q^2$ is transported by the turbulence either toward $(V_{q^2} < 0)$ or away from $(V_{q^2} > 0)$ the wall; it is plotted in figure 7(*b*). Unlike in the Schwarz & Bradshaw curved-duct experiment, where V_{q^2} was observed to decrease near the wall as the crossflow developed, and increase farther away, only minimal changes are produced by the Case S45 skewing. The source of this discrepancy is thought to be the off-centreline streamwise acceleration/deceleration, mentioned above, found in the duct flow (see also figure 18*b* below). The DNS results reveal that the impact of the pure skewing strain upon the turbulence structure is limited. Some aspects of modelling 3DWLs are therefore likely to be influenced less by mean three-dimensionality than by features unrelated to the introduction of mean crossflow.

An attribute of the pure-skewing flow that *will* expose many turbulence models – any that assume isotropic eddy viscosity – is the lack of agreement between the direction of the mean shear and Reynolds shear stress. Differences as large as 30° are observed, especially near the wall. This can be seen in figure 8. The sign change in the mean gradient angle $\gamma_g = \arctan[(\partial\overline{w}/\partial y)/(\partial\overline{u}/\partial y)]$ in figure 8(*a*) is a consequence of the sign change in $\partial\overline{w}/\partial y$ observed in figure 4(*a*). The modelling difficulty is in the finite time required for the spanwise shear to produce spanwise Reynolds stress $-\overline{v'w'}$. The slow growth of $-\overline{v'w'}$ is another classical feature of non-stationary 3DBLs (Schwarz & Bradshaw 1994). Because of it, the stress angle $\gamma'_\tau = \arctan[-\overline{v'w'}/-\overline{u'v'}]$ lags well behind γ_g. In fact, early on in the outer region the gradient and stress angles have opposite signs, and therefore rotate away from each other; it is only much later

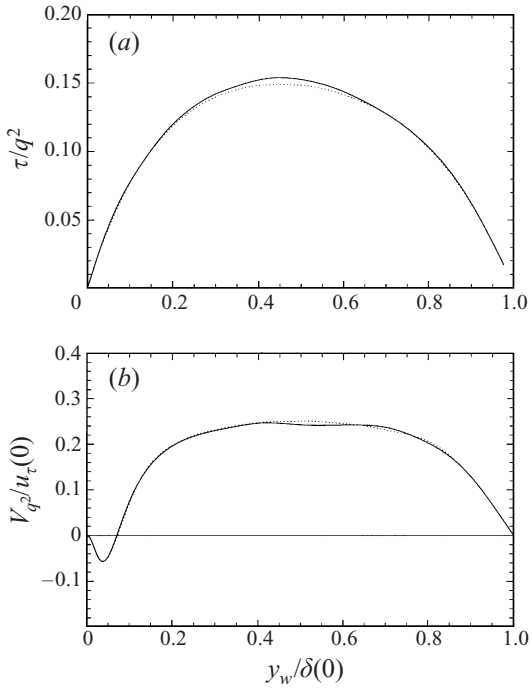

FIGURE 7. Profiles of (*a*) stress/energy ratio $a_1 = \tau/q^2$ and (*b*) turbulent transport velocity $V_{q^2} = \overline{v'u_i'u_i'}/q^2$ for Case S45: ——, $\mathscr{A}_{13}t = 0$ ($\alpha = 0°$); ·····, $\mathscr{A}_{13}t = 0.125$ ($\alpha = 7°$) (data for $\mathscr{A}_{13}t = 0.0625$ not shown to clarify presentation). Reynolds-stress magnitude $\tau = (\overline{u'v'}^2 + \overline{v'w'}^2)^{1/2}$.

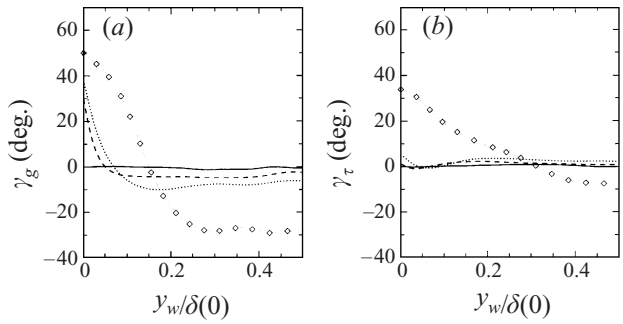

FIGURE 8. Direction of (*a*) mean shear γ_g and (*b*) Reynolds shear stress γ_τ for Case S45: ——, $\mathscr{A}_{13}t = 0$ ($\alpha = 0°$); - - - -, $\mathscr{A}_{13}t = 0.0625$ ($\alpha = 3.6°$); ·····, $\mathscr{A}_{13}t = 0.125$ ($\alpha = 7°$); ◇, $\mathscr{A}_{13}t = 0.60$ (single realization). Mean-shear angle $\gamma_g = \arctan[(\partial\overline{w}/\partial y)/(\partial\overline{u}/\partial y)]$; Reynolds-stress angle $\gamma_\tau' = \arctan[-\overline{v'w'}/-\overline{u'v'}]$.

that γ_τ begins to follow (i.e. have the same sign but a smaller value than) γ_g in the outer region (compare the open symbols in figures 8(*a*) and 8(*b*), which show the variation of γ_g and γ_τ at $\mathscr{A}_{13}t = 0.60$). One of the primary goals of this project is to more fully understand the relationship between the mean shear $(\partial\,\overline{u}/\partial y, \partial\,\overline{w}/\partial y)$ and the $(-\overline{u'v'}, -\overline{v'w'})$ stresses, and to ascertain the implications for modelling suddenly distorted 3DBLs. This will require consideration of the behaviour of the various terms in the Reynolds-stress budget equations, the subject to which we now turn.

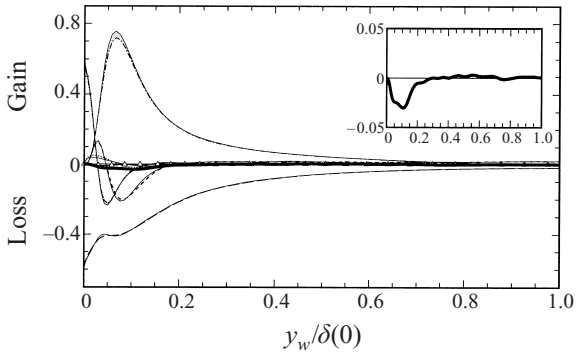

FIGURE 9. Terms in the budget of turbulence kinetic energy $k = 0.5\overline{u_i' u_i'}$ for Case S45: thin solid curves (——) denote terms at $\mathscr{A}_{13}t = 0$ (before strain); —·—, $P_k^S = \frac{1}{2}P_{ii}^S$ at $\mathscr{A}_{13}t = 0.125$; – – – –, $-\varepsilon_k = -\frac{1}{2}\varepsilon_{ii}$ at $\mathscr{A}_{13}t = 0.125$; - - - -, $T_k = \frac{1}{2}T_{ii}$ at $\mathscr{A}_{13}t = 0.125$; —··—, $D_k = \frac{1}{2}D_{ii}$ at $\mathscr{A}_{13}t = 0.125$; ·····, $\Pi_k = \frac{1}{2}\Pi_{ii}$ at $\mathscr{A}_{13}t = 0.125$; △, $P_k^{\mathscr{A}} = \frac{1}{2}P_{ii}^{\mathscr{A}}$ at $\mathscr{A}_{13}t = 0.125$; thick solid curve (——), sum of all terms ($\approx \partial k/\partial t$) at $\mathscr{A}_{13}t = 0.125$ (also shown in inset with expanded vertical scale). Shaded regions indicate change from unstrained initial-condition profiles. Curves normalized by U_{ref}^4/ν, where $U_{\mathrm{ref}} = 0.73u_\tau(0)$.

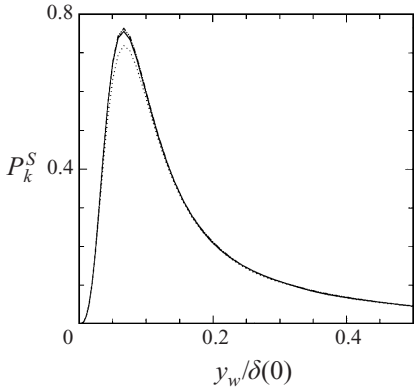

FIGURE 10. Mean-shear production $P_k^S = -\overline{u'v'}\,\partial\,\overline{u}/\partial y - \overline{v'w'}\,\partial\,\overline{w}/\partial y$ of turbulence kinetic energy for Case S45: ——, P_k^S at $\mathscr{A}_{13}t = 0$; ·····, P_k^S at $\mathscr{A}_{13}t = 0.125$; —··—, product of $-\overline{u'v'}$ at $\mathscr{A}_{13}t = 0$ and $\partial\,\overline{u}/\partial y$ at $\mathscr{A}_{13}t = 0.125$. Normalization as in figure 9.

3.1.2. *Reynolds-stress budgets*

For the strained-channel flow, the non-dimensionalized transport equations for the Reynolds stresses reduce to

$$\frac{\partial \overline{u_i' u_j'}}{\partial \widehat{t}} = P_{ij} + T_{ij} + D_{ij} + \Pi_{ij} - \varepsilon_{ij}, \tag{3.2}$$

where the effective material derivative $\partial/\partial\widehat{t} = \partial/\partial t + \mathscr{A}_{22} y \partial/\partial y$ (see § 2), and right-hand-side terms are the rates of (cf. Mansour, Kim & Moin 1988)

$$\text{production}: \; P_{ij} = -\overline{u_i' v'}\,\frac{\partial\,\overline{u}_j}{\partial y} - \overline{u_j' v'}\,\frac{\partial\,\overline{u}_i}{\partial y} - \overline{u_i' u_\ell'}\mathscr{A}_{j\ell} - \overline{u_j' u_\ell'}\mathscr{A}_{i\ell},$$

$$\text{dissipation}: -\varepsilon_{ij} = -\frac{2}{Re}\,\overline{\frac{\partial u_i'}{\partial x_\ell}\frac{\partial u_j'}{\partial x_\ell}},$$

$$\text{turbulent transport}: \; T_{ij} = -\frac{\partial}{\partial y}\left(\overline{v' u_i' u_j'}\right),$$

$$\text{viscous diffusion}: \; D_{ij} = \frac{1}{Re}\frac{\partial^2}{\partial y^2}\left(\overline{u_i' u_j'}\right),$$

$$\text{velocity–pressure-gradient term}: \; \Pi_{ij} = -\left(\overline{u_i' \frac{\partial p'}{\partial x_j}} + \overline{u_j' \frac{\partial p'}{\partial x_i}}\right).$$

The Reynolds number Re is again based on the reference velocity U_{ref} and $\delta(0)$, the channel half-width of the unstrained initial condition. For Cases S45 and AS45, $Re = 130$ and U_{ref} is 0.73 times the initial friction velocity $u_\tau(0)$, such that $Re_\tau = u_\tau \delta / \nu = (u_\tau / U_{\mathrm{ref}})\, Re \exp(\mathscr{A}_{22} t)$ is initially ≈ 180 (as in Kim *et al.* 1987 and Mansour *et al.* 1988). The velocity u_i' and kinematic pressure p' in (3.2) have been scaled by U_{ref}, while the independent variable x_i is in units of $\delta(0)$. The Reynolds stresses $\overline{u_i' u_j'}$ are functions solely of time $t = \widehat{t}$ and the wall-normal coordinate y, or equivalently the distance from the nearest wall, $y_w(t) = (1 - |y(0)|) \exp(\mathscr{A}_{22} t) = y_w(0) \exp(\mathscr{A}_{22} t)$.

Some modellers replace the velocity–pressure-gradient term in (3.2) by $\Pi_{ij} = \psi_{ij} + \phi_{ij}$, where (for this parallel flow) $\psi_{ij} = -(\partial \overline{p' u_i'} / \partial y)\delta_{2j} - (\partial \overline{p' u_j'} / \partial y)\delta_{2i}$ is the pressure–transport correlation (δ_{ij} is the Kronecker delta), and $\phi_{ij} = \overline{(p'(\partial u_i'/\partial x_j + \partial u_j'/\partial x_i))}$ is the pressure–strain term. We focus primarily upon the original velocity–pressure-gradient correlation Π_{ij} in this discussion.

On the other hand, a decomposition is applied to the production term, in order to distinguish between the direct effects of the irrotational applied strain $\mathscr{A}_{ij}$ and those arising indirectly through changes to the rotational mean $\overline{\boldsymbol{u}}(y,t)$. We separate the total production rate P_{ij} into rotational (i.e. shear) and irrotational (applied-strain) components, $P_{ij} = P_{ij}^s + P_{ij}^{\mathscr{A}}$ respectively, where

$$P_{ij}^s = -\overline{u_i' v'}\,\frac{\partial \overline{u}_j}{\partial y} - \overline{u_j' v'}\,\frac{\partial \overline{u}_i}{\partial y}, \tag{3.3a}$$

$$P_{ij}^{\mathscr{A}} = -\overline{u_i' u_\ell'}\,\mathscr{A}_{j\ell} - \overline{u_j' u_\ell'}\,\mathscr{A}_{i\ell}. \tag{3.3b}$$

We begin by examining the budget of turbulence kinetic energy with the aim of determining the source of the reduction observed when the pure-skewing strain is applied (cf. figure 6*b*). The shaded regions in figure 9 indicate the amount each term changes during the time from $\mathscr{A}_{13} t = 0$ to 0.125, while the thick solid curve (both on the main plot and the expanded-scale inset) denotes the negative net $\partial k / \partial t$ given by the sum of all the right-hand-side terms† at $\mathscr{A}_{13} t = 0.125$. Also shown (the open symbols) is the 'new' applied-strain production $P_k^{\mathscr{A}} = -2\overline{u'w'}\mathscr{A}_{13}$; it is initially negligible (identically zero in the two-dimensional limit), and is still very small at $\mathscr{A}_{13} t = 0.125$, since by this time the applied strain has yet to produce an appreciable $-\overline{u'w'}$ stress. Although $P_k^{\mathscr{A}}$ contributes slightly to the kinetic energy decrease, the major source of the reduction is the change incurred by the mean-shear production $P_k^s = -\overline{u'v'}\,\partial \overline{u}/\partial y - \overline{v'w'}\,\partial \overline{w}/\partial y$. Most of the P_k^s decrease can in turn be traced to a reduction in the streamwise Reynolds shear stress $-\overline{u'v'}$, as figure 10 illustrates. The $\mathscr{A}_{13}$-induced decrease of the shear production is affected more by changes to the

† Strictly speaking, the right-hand-side sum is only approximately equal to $\partial k / \partial t$, since it includes any errors due to spatial discretization and incomplete statistical convergence. But for all budget data presented herein these factors are small enough that in the discussion to follow the approximation can be taken as an identity.

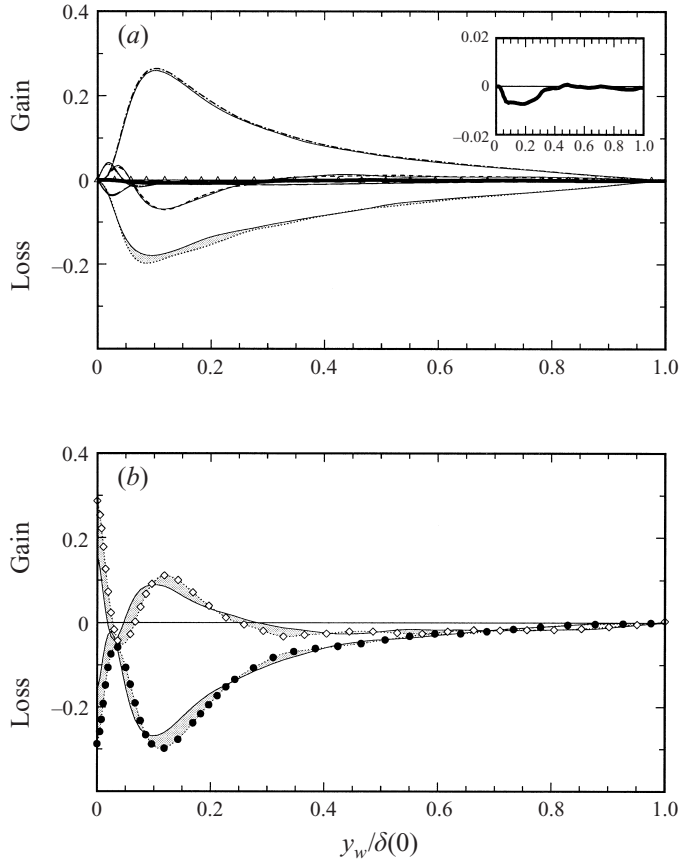

FIGURE 11. Terms in the budget of streamwise Reynolds shear stress $-\overline{u'v'}$ for Case S45: thin-solid curves (——) in (*a*) and (*b*) denote terms at $\mathscr{A}_{13}t = 0$ (before strain); —·—, $-P_{12}^s$ at $\mathscr{A}_{13}t = 0.125$; – – – –, $+\varepsilon_{12}$ at $\mathscr{A}_{13}t = 0.125$; - - - -, $-T_{12}$ at $\mathscr{A}_{13}t = 0.125$; —··—, $-D_{12}$ at $\mathscr{A}_{13}t = 0.125$; ·····, $-\Pi_{12}$ at $\mathscr{A}_{13}t = 0.125$; △, $-P_{12}^{\mathscr{A}}$ at $\mathscr{A}_{13}t = 0.125$; thick solid curve (——), sum of all terms ($\approx -\partial\overline{u'v'}/\partial t$) at $\mathscr{A}_{13}t = 0.125$ (also shown in inset with expanded vertical scale). Part (*b*) symbols: ●, pressure–strain correlation $-\phi_{12}$ at $\mathscr{A}_{13}t = 0.125$; ◇, pressure–transport term $-\psi_{12}$ at $\mathscr{A}_{13}t = 0.125$. Shaded regions in (*a*) and (*b*) indicate change from unstrained initial-condition profiles. Normalization as in figure 9.

$-\overline{u'v'}$ Reynolds stress than to the $\partial\,\overline{u}/\partial y$ profile – since the initial P_k^s (the solid curve in figure 10) is nearly the same as the hypothetical production (the chain-double-dot curve) defined by the product of the mean shear $\partial\,\overline{u}/\partial y$ at $\mathscr{A}_{13}t = 0.125$ and the initial value of $-\overline{u'v'}$.

This result leads us to consider the $-\overline{u'v'}$ budget, whose terms are plotted in figure 11. The shaded regions again indicate the amount each term has changed with respect to its initial profile. Here the primary reason why $-\partial\,\overline{u'v'}/\partial t$ is negative (see the thick solid curve inset on the upper right-hand side of the figure) is the increase in amplitude of the velocity–pressure-gradient correlation Π_{12} (dotted curve). The rapid temporal variation of Π_{12} is accompanied by even larger changes to the pressure–strain ϕ_{12} and pressure–transport ψ_{12} terms, of which it is the sum (figure 11*b*). This implies that for this flow the velocity–pressure-gradient correlation, since it represents the imbalance of two larger terms, might be easier to model than each of ψ_{12} and ϕ_{12}.

The outer-layer increase in $-\overline{u'v'}$ production, $-P_{12}^s = \overline{v'v'}\partial\,\overline{u}/\partial y$, (barely) visible in

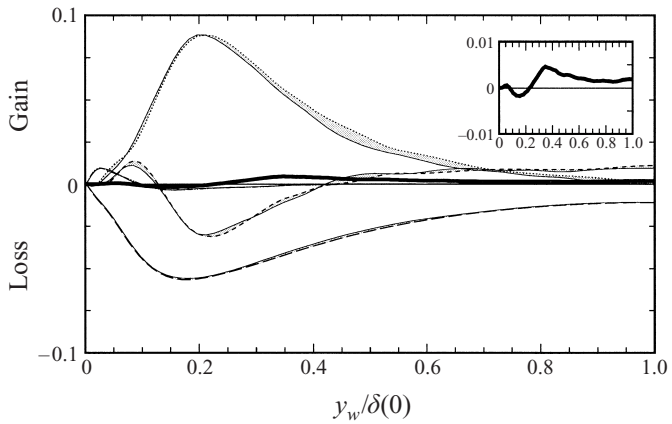

FIGURE 12. Terms in the budget of vertical-velocity variance $\overline{v'v'}$ for Case S45: thin solid curves (——) denote terms at $\mathscr{A}_{13}t = 0$ (before strain); – – – –, $-\varepsilon_{22}$ at $\mathscr{A}_{13}t = 0.125$; - - - -, T_{22} at $\mathscr{A}_{13}t = 0.125$; —··—, D_{22} at $\mathscr{A}_{13}t = 0.125$; ·····, Π_{22} at $\mathscr{A}_{13}t = 0.125$; thick solid curve (——), sum of all terms ($\approx \partial\overline{v'v'}/\partial t$) at $\mathscr{A}_{13}t = 0.125$ (also shown in inset with expanded vertical scale). Shaded regions indicate change from unstrained initial-condition profiles. Normalization as in figure 9.

figure 11 is due in large part to amplification of Π_{22}, and the $\partial\overline{v'v'}/\partial t > 0$ it causes in this region (figure 12) – although changes to the dissipation ε_{22} and especially the turbulence transport T_{22} are not negligible. We conclude that the most apparent changes to the Reynolds-stress tensor crucially depend on the velocity–pressure-gradient correlation; the near-wall stabilization of the turbulence demonstrated in figure 5 can thus be attributed to the interaction of the pressure and velocity fluctuations overwhelming the influence of the extra-strain production introduced by the mean spanwise shear.

The Π_{ij} term also accounts for the slow growth of the spanwise Reynolds shear stress $-\overline{v'w'}$ (and its unexpected sign in the outer region, opposite to that of $\partial\overline{w}/\partial y$), and the resulting large difference documented in figure 8 between the direction of the mean gradient $(\partial\overline{u}/\partial y, \partial\overline{w}/\partial y)$ and that of the shear stress $(-\overline{u'v'}, -\overline{v'w'})$. Evidence is presented in figure 13, which shows how the $-\overline{v'w'}$ budget is affected by the $\mathscr{A}_{13}$ skewing. Two terms respond immediately to the impulsively applied strain: the applied-strain production $P_{23}^{\mathscr{A}}$ and the velocity–pressure-gradient correlation Π_{23}. The other terms in (3.2) react over finite time. These two quantities therefore alter the balance of the $-\overline{v'w'}$ transport equation the moment the strain is applied; they adjust from being either exactly zero ($P_{23}^{\mathscr{A}}$) or approximately so (Π_{23}, to the extent that the initial-condition statistics are converged and purely two-dimensional) to the initial $\mathscr{A}_{13}$-induced values illustrated in figure 13(*a*). The open-symbol curve denotes the new explicit production of $-\overline{v'w'}$, $-P_{23}^{\mathscr{A}} = \overline{u'v'}\mathscr{A}_{13}$, while the dotted curve shows the increase of $-\Pi_{23}$ due solely to the initial 'turning on' of the applied strain. (To clarify the presentation, the $-\Pi_{23}$ increase is measured with respect to its unstrained initial value, since the latter is not identically zero, and contains statistically insignificant but noticeable oscillations when viewed on the scale used for figure 13*a*.) The shaded region in figure 13(*a*) represents the sum of these two 'initial pulse' terms. We see that the initial (impulsive) effect of the strain is to create positive $-\overline{v'w'}$ everywhere except near the wall, where the trend is $-\partial\overline{v'w'}/\partial y < 0$. This tendency is exactly opposite to that associated with mean-shear production $-P_{23}^{S}$ (see the chain-dot curve in figure 13*b*) defined by the spanwise-shear profile (cf. figure 4*a*). This explains why initially

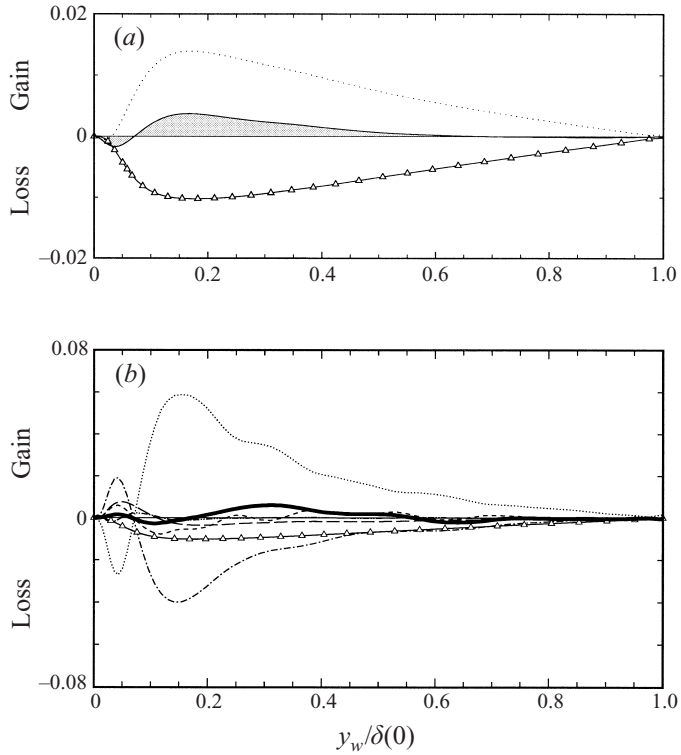

FIGURE 13. Terms in the budget of spanwise Reynolds shear stress $-\overline{v'w'}$ for Case S45 at (*a*) $\mathscr{A}_{13}t = 0$ (immediately after pure-skewing strain applied) and (*b*) $\mathscr{A}_{13}t = 0.125$ for Case S45: —·—, $-P^S_{23}$; ————, $+\varepsilon_{23}$; - - - -, $-T_{23}$; —··—, $-D_{23}$; ·····, $-\Pi_{23}$; △, $-P^{\mathscr{A}}_{23}$; thick solid curve (——), sum of all terms ($\approx -\partial\overline{v'w'}/\partial t$) at $\mathscr{A}_{13}t = 0.125$. Solid curve (——) and shaded region in (*a*) indicate net imbalance initially supplied by sum of $-P^{\mathscr{A}}_{23}$ and $-\Pi_{23}$ (i.e. the terms instantly affected by applied strain); unstrained initial-field profile subtracted from $-\Pi_{23}$ in (*a*) to remove statistically insignificant oscillations. (Note difference in vertical scales of *a* and *b*.) Normalization as in figure 9.

the mean-gradient γ_g and shear-stress γ_τ angles shown in figure 8 have opposite signs in the outer layer. In general, $-\Pi_{23}$ and $-P^s_{23}$ tend to oppose each other, with their magnitudes each much larger than the explicit production $-P^{\mathscr{A}}_{23}$, and especially the net growth rate $-\partial\overline{v'w'}/\partial t$. The budget of spanwise-shear stress $-\overline{v'w'}$, and the others examined in this section, therefore indicates that correctly accounting for the velocity–pressure-gradient terms will be a strategic part of accurately modelling perturbed 3DBLs.

3.2. *Swept-wing strain: Case AS45*

Three-dimensionality rarely occurs in isolation, since pressure gradients that introduce a mean crossflow usually also accelerate or decelerate the boundary layer. Classic examples include flows upstream of wing–body junctions, over swept airfoils, and within the curved passages of turbomachinery – each of which in addition to being subject to a pure-skewing outer-layer deformation also experiences mean stretching or compression in the streamwise and wall-normal directions (van den Berg *et al.* 1975; Bradshaw & Pontikos 1985; Anderson & Eaton 1989; Ölçmen & Simpson 1995). In the past it has been difficult to differentiate between behaviour driven by the off-diagonal and the normal components of the irrotational deformation. The

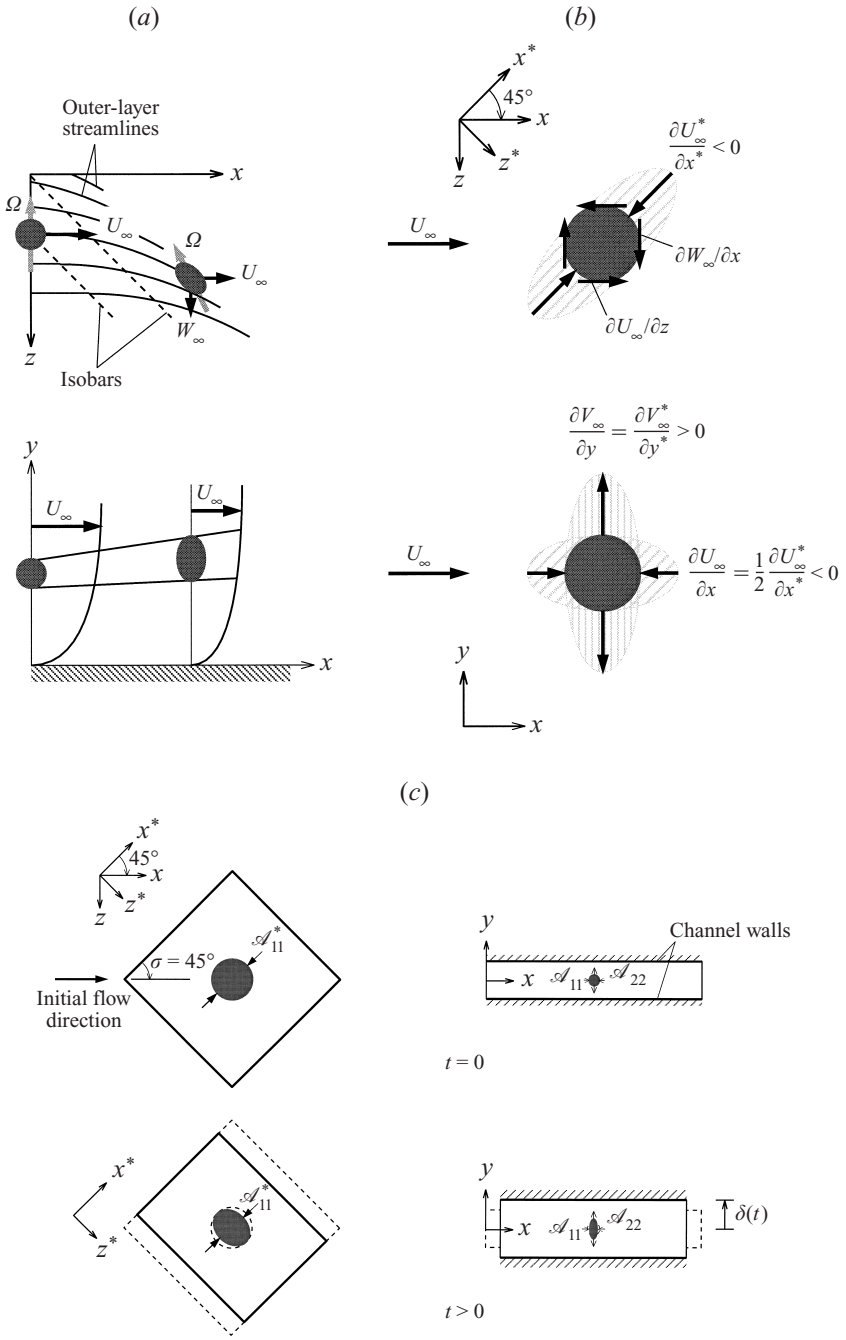

FIGURE 14. Plan and side views of three-dimensional boundary layer subjected to combined pure-skewing and APG strain. (*a*) Spatially developing flow: 45° infinite-swept wing ('port-side' version). (*b*) Strain applied to fluid element at $x = 0$ of spatially developing flow and at $t = 0$ of strained channel DNS. (Cross-hatched regions represent angular distribution of normal strains.) (*c*) Initial and deformed domain of strained-channel DNS for Case AS45.

DNS data presented in this section, from Case AS45, address this difficulty. By subjecting wall-bounded turbulence to the most general strain allowed by (2.1) – and thereby combining the effects of spanwise and streamwise mean pressure gradients – and comparing the results to those from the pure-skewing simulation, we expect to obtain significant insight into the physics of non-stationary 3DBLs.

We choose strain-field parameters that correspond to a time-developing counterpart of the infinite-swept-wing experiments of van den Berg *et al.* (1975) and Bradshaw & Pontikos (1985). Consequently, the principal-strain components are defined as $\mathscr{A}^*_{11} = -\mathscr{A}^*_{22} = -1.47u_\tau(0)/\delta(0)$ and $\mathscr{A}^*_{33} = 0$. Rather than the 35° angle of sweep used in the experiments, for Case AS45 σ is set to 45°. As a result, we apply the spanwise skewing, streamwise and spanwise deceleration, and wall-normal stretching appropriate for a 45° swept-wing: $\mathscr{A}_{13} = -\mathscr{A}_{11} = -\mathscr{A}_{33} = 0.5\mathscr{A}_{22} > 0$ (see table 1 and figure 14). The strain rate for this case is about an order of magnitude larger than that imposed in the van den Berg *et al.* and Bradshaw & Pontikos experiments (measured in terms of the friction velocity and boundary-layer thickness at the inlet of their curved diffuser), where here $\mathscr{A}_{13} = 0.735$ of the initial u_τ/δ. Note that the magnitude of skewing $\mathscr{A}_{13}$ is the same for Case AS45 as it was for Case S45. (While the computational expense required to consider the experimental strain rate for the same range of $A_{13}t$ would have been unrealistically high, the early stages of one realization from a simulation with strain rate approximately equal to the van den Berg *et al.* and Bradshaw & Pontikos values will also be briefly discussed.) The ratio of mean-distortion to turbulence timescales will thus be significantly different in the strained-channel and experimental flows. Because of these factors, we only anticipate qualitative agreement.

3.2.1. *Mean profiles and histories*

The development of the Case AS45 mean crossflow is compared to that for the non-APG strain in figures 15(*a*) and 15(*b*). (Contrast the curves without and with symbols.) The total strain for the last time shown, $\mathscr{A}_{13}t = 0.125$, is similar to the equivalent total strain ($\mathscr{A}_{13}t \approx 0.15$) imposed in the Bradshaw & Pontikos experiment. While both DNS flows experience mean spanwise shear $\partial\overline{w}/\partial y$ in the outer layer as a result of the skewing, the distorting effect of the APG is also apparent for Case AS45, in the increase with time of the distance between the channel walls, which duplicates the thickening of the layer caused by the mean streamwise deceleration. In other words, $\partial\overline{w}/\partial y$ is distributed over a wider and wider region as time passes. The agreement with the SWH prediction (the solid lines in figure 15*b*) is not diminished by the presence of the APG strain. The streamwise deceleration $\mathscr{A}_{11} < 0$ is responsible for the leftward shift of the hodograph as the difference between the mean streamwise velocities of the flow and the wall is driven toward zero, under the influence of the in-plane wall motion prescribed by equation (2.14). For Case AS45, the streamwise and spanwise components of the centreline–wall velocity differences invoked by (2.14) are

$$\frac{\overline{u}_c(t) - u_w(t)}{\overline{u}_c(0)} = \tfrac{1}{2}(1 + \exp(-2\mathscr{A}_{13}t)), \tag{3.4a}$$

$$\frac{\overline{w}_c(t) - w_w(t)}{\overline{u}_c(0)} = \tfrac{1}{2}(1 - \exp(-2\mathscr{A}_{13}t)). \tag{3.4b}$$

As indicated in figure 16(*a*) (a graphical presentation of (3.4)), the wall motion thus combines a bulk streamwise deceleration (upper solid curve) with a growing crossflow

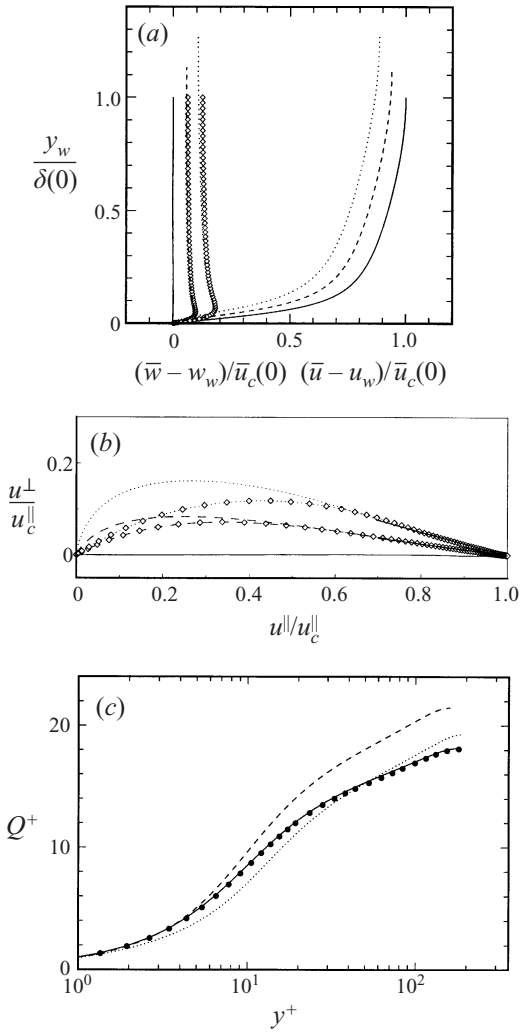

FIGURE 15. Mean velocity evolution for Case AS45 (coordinates and normalization as in figure 4): ——, $\mathscr{A}_{13}t = 0$ ($\alpha = 0°$) (and SWH prediction in *b*); - - - -, $\mathscr{A}_{13}t = 0.0625$ ($\alpha = 3.6°$); ·····, $\mathscr{A}_{13}t = 0.125$ ($\alpha = 7°$); ●, two-dimensional $Re_\tau = 180$ channel of Kim *et al.* (1987). Open symbols in (*a*) and (*b*) are $\mathscr{A}_{13}t = 0.0625$ and 0.125 results from Case S45.

(lower solid curve). The strategy of coupling the in-plane wall motion and outer-layer strain described in § 2 produces the desired mean flow behaviour.

The effect of the mean deceleration can be seen in the local minima in the total-shear-stress profile plotted in figure 17(*a*), and even more directly in the streamwise skin-friction history given by the upper thin solid curve in figure 16(*b*). As one would expect for a flow with negative $\mathscr{A}_{11}$, the surface shear exhibits a rapid decrease of the streamwise component. (The open symbols in figure 16 again represent the Case S45 results.) At $\mathscr{A}_{13}t = 0.125$, the latest time for which flow statistics are examined, the streamwise skin friction has fallen to 7.5% of its initial value, before becoming zero near $\mathscr{A}_{13}t = 0.15$ (and entering a 'pseudo-separation' regime, in the sense that the skin-friction reversal is not accompanied by strong flow away from the wall as it is in the spatial case). Despite undergoing such a large reduction, the mean streamwise

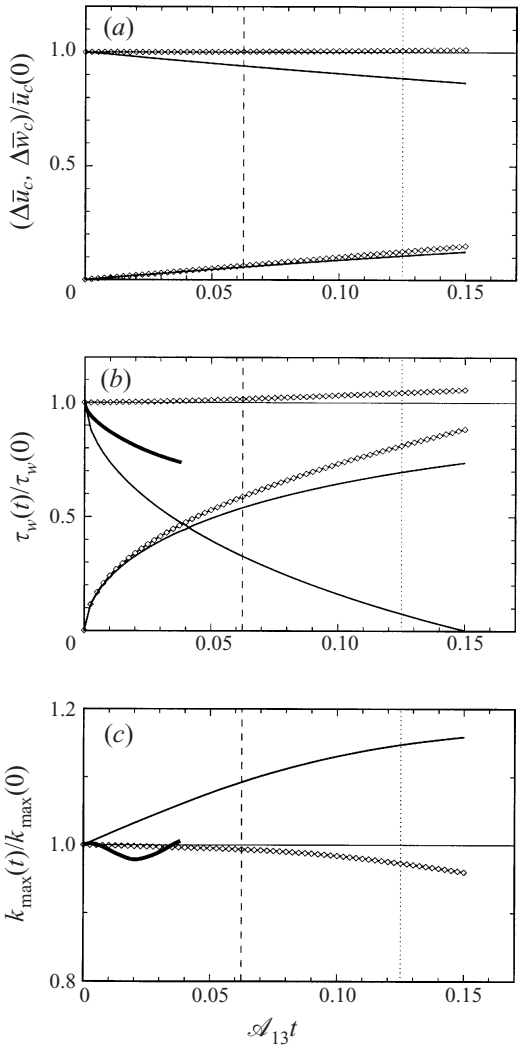

FIGURE 16. Histories of (*a*) mean centreline–wall velocity difference (equation (3.4)), (*b*) surface shear stress and (*c*) maximum turbulence kinetic energy for Case AS45: upper curves, streamwise components ($\Delta\overline{u}_c = \overline{u}_c - u_w$ in (*a*), $(\tau_w)_x = \nu(\partial\,\overline{u}/\partial y)_w$ in (*b*)); lower curves, spanwise component ($\Delta\overline{w}_c = \overline{w}_c - w_w$ and $(\tau_w)_z = \nu(\partial\,\overline{w}/\partial y)_w$). Thin solid curve in (*c*) indicates maximum over all y_w locations of $k = \frac{1}{2}\overline{u_i' u_i'}$ (cf. figure 17*b*); thick solid curves in (*b*) and (*c*) are from a single realization with $\mathscr{A}_{13} = -\mathscr{A}_{11} = -\mathscr{A}_{33} = 0.5\mathscr{A}_{22} = 0.12u_\tau(0)\,/\delta(0)$ (i.e. each component 16% of that used for Case AS45) (note expanded vertical scale in *c*). Vertical lines mark times for which mean profiles are shown in other figures. Open symbols are from Case S45.

shear at the wall $(\partial\,\overline{u}/\partial y)_w$ at $\mathscr{A}_{13}t = 0.125$ remains 18 times the size of the applied skewing strain $\mathscr{A}_{13}$. This suggests that in the near-wall region any unphysical effects due to the strain-induced deformation of the no-slip walls are less important at $\mathscr{A}_{13}t = 0.125$ than are features associated with the streamwise and spanwise shear.

By the time $(\partial\,\overline{u}/\partial y)_w$ changes sign at $\mathscr{A}_{13} \approx 0.15$, the mean flow has decelerated to the point where $(\overline{u}_c - \overline{u}_c(0)\,)/\overline{u}_c(0) \approx 0.85$, and the effective pressure coefficient, $(C_p)_{\rm eff} \equiv 1 - (\overline{u}_c/\overline{u}_c(t)\,)^2$ is less than 0.3. Separation usually occurs when $(C_p)_{\rm eff}$ is between 0.45 and 0.50 (e.g. Alving & Fernholz 1995; Spalart & Coleman 1997). The

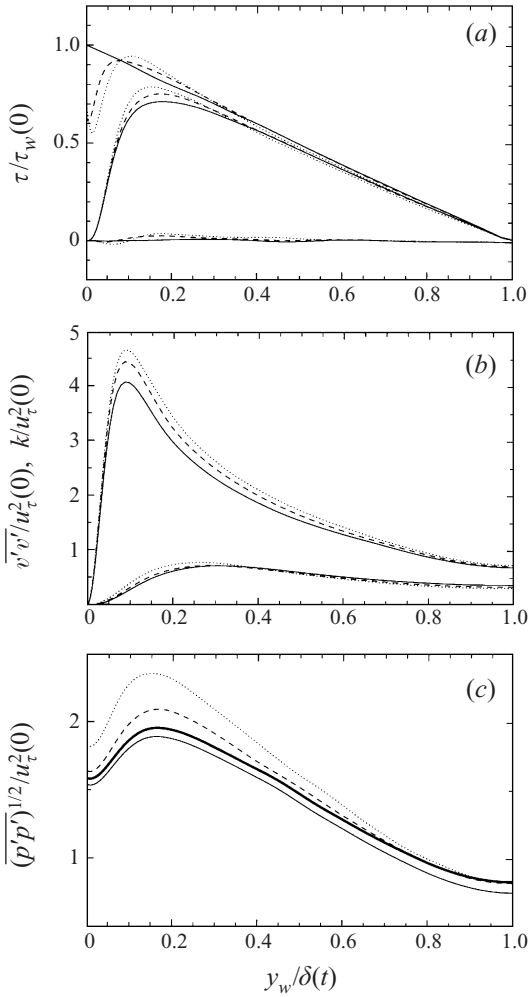

FIGURE 17. Profiles of (*a*) shear stress, (*b*) turbulence kinetic energy, and (*c*) root-mean-square pressure fluctuations for Case AS45: ——, $\mathscr{A}_{13}t = 0$ ($\alpha = 0°$); - - - -, $\mathscr{A}_{13}t = 0.0625$ ($\alpha = 3.6°$); ·····, $\mathscr{A}_{13}t = 0.125$ ($\alpha = 7°$). Lower, middle, and upper curves in (*a*) respectively correspond to spanwise Reynolds shear stress $-\overline{v'w'}$, streamwise Reynolds shear stress $-\overline{u'v'}$, and total shear stress $(\tau)_{\text{total}} = [(\nu(\partial\,\overline{u}/\partial y) - \overline{u'v'})^2 + (\nu(\partial\,\overline{w}/\partial y) - \overline{v'w'})^2]^{1/2}$. Thick solid (——) curve in (*c*) is $\mathscr{A}_{13}t = 0$ value immediately after strain is applied (note expanded vertical scale).

lower-than-usual $(C_p)_{\text{eff}}$ at separation may be influenced by the step-function strain history. It is more strongly affected by the magnitude of the applied strain: when another infinite-swept-wing strain is used, one with $\mathscr{A}_{13}$ ($= |\mathscr{A}_{11}| = \frac{1}{2}\mathscr{A}_{22} = |\mathscr{A}_{33}|$) approximately the same fraction of $u_\tau(0)/\delta(0)$ as in the van den Berg *et al.* and Bradshaw & Pontikos experiments (such that each component is 16% of its Case AS45 value), the streamwise wall-shear history shown by the thick-solid curve in figure 16(*b*) results. Although it has been stopped before the streamwise wall shear τ_w becomes negative, this run shows that the time at which it will do so is well past the $\mathscr{A}_{13}t = 0.15$ (and therefore significantly greater than the $(C_p)_{\text{eff}} \approx 0.3$) found for Case AS45. The separation point is not fixed solely by the magnitude of the pressure coefficient.

Whereas the effect of the swept-wing strain field is stabilizing near the wall (in the sense that it diminishes $\partial\,\overline{u}/\partial y$ and therefore the production), farther away the

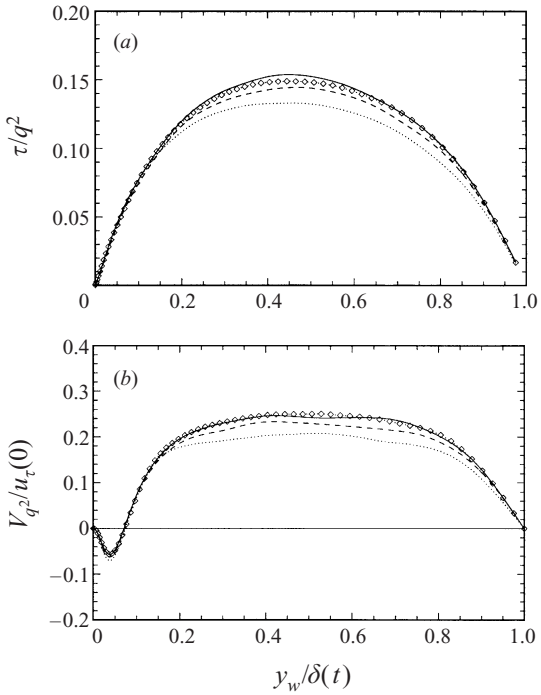

FIGURE 18. Profiles of (*a*) stress/energy ratio $a_1 = \tau/q^2$ and (*b*) turbulent transport velocity $V_{q^2} = \overline{v'u_i'u_i'}/q^2$ for Case AS45: ——, $\mathscr{A}_{13}t = 0$ ($\alpha = 0°$); - - - -, $\mathscr{A}_{13}t = 0.0625$ ($\alpha = 3.6°$); ·····, $\mathscr{A}_{13}t = 0.125$ ($\alpha = 7°$). Open symbols in (*a*) and (*b*) are $\mathscr{A}_{13}t = 0.125$ results from Case S45.

opposite is true. Figure 16(*c*) shows that the maximum turbulence kinetic energy $k_{\max}$ increases monotonically in time, with non-zero initial slope. This positive $\partial k_{\max}/\partial t$ at $t = 0$ is another symptom of the relatively large Case AS45 strain rate; for the run with $\mathscr{A}_{13}$ chosen to approximate the experiments, the peak k initially decreases (cf. the thick solid curve in figure 16(*c*) with figure 7(*g*) of Bradshaw & Pontikos 1985). The Case AS45 strain is responsible for an increase in turbulence activity not just at the location of largest k, but across the entire channel: the kinetic-energy profiles in figure 17(*b*) show that k increases at every y_w. (Using the time-dependent channel half-width $\delta(t)$ to non-dimensionalize the wall-normal coordinate in figure 17(*b*) has made the outward shift of the location of maximum turbulence kinetic energy, typical of APG layers, less obvious; replacing $\delta(t)$ with the constant initial value $\delta(0)$ produces the expected behaviour, at least its initial stage; cf. figure 15*a*.) The wall-normal fluctuations $\overline{v'v'}$, on the other hand, increase their peak value while becoming less intense near the centreline (figure 17*b*). The pressure disturbances, like k, also uniformly increase for $0 \leqslant y_w \leqslant \delta(t)$ (figure 17*c*), to levels significantly larger than those found for Case S45. The impulsive change to the initial pressure field observed just after the strain is applied is also more pronounced for the swept-wing strain (compare the thick solid curves in figures 17*c* and 6*c*). In spite of the near-wall reduction in $\partial\,\overline{u}/\partial y$ revealed in figure 16(*b*), the streamwise Reynolds stress $-\overline{u'v'}$ experiences rapid growth for $y_w \leqslant 0.3\delta(t)$, where $-\partial\,\overline{u'v'}/\partial t > 0$. At larger distances from the wall $-\overline{u'v'}$ decreases slightly over time. An explanation for the behaviour of the k, $\overline{v'v'}$, and $-\overline{u'v'}$ statistics (and of the spanwise stress $-\overline{v'w'}$) presented in figure 17 is deferred until the next subsection, where we examine the Reynolds-stress budgets.

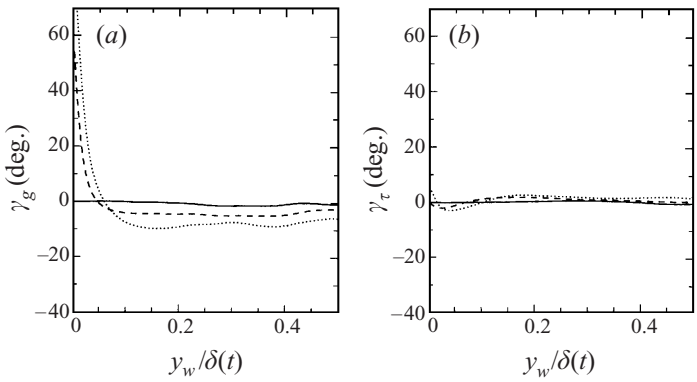

FIGURE 19. Direction of (*a*) mean shear γ_g and (*b*) Reynolds shear stress γ_τ for Case AS45: ——, $\mathscr{A}_{13}t = 0$ ($\alpha = 0°$); - - - -, $\mathscr{A}_{13}t = 0.0625$ ($\alpha = 3.6°$); ·····, $\mathscr{A}_{13}t = 0.125$ ($\alpha = 7°$).

One can obtain insight into the relative significance of the various strain components by comparing the evolution of the stress/energy ratio a_1 and the turbulent transport velocity V_{q^2} for Case AS45 with those for Case S45. Both quantities are reduced in the outer layer to well below their initial levels by the swept-wing strain; a_1 and V_{q^2} reductions of the same magnitude were also found in the outer layer of the Bradshaw & Pontikos flow. Figure 18 also shows that the deformation containing normal-strain components (i.e. the one corresponding to an adverse streamwise pressure gradient) produces a much greater decrease than when the mean skewing acts alone (the open symbols in figure 18 represent pure-skewing results at $\mathscr{A}_{13}t = 0.125$, which corresponds to the dotted-profile Case AS45 data.) This implies that the strain created by an adverse pressure gradient has a greater influence on the development of the turbulence in a three-dimensional boundary layer than the spanwise shear does. Because of its wide-ranging practical consequences (e.g. with regard to turbulence-model development), we consider this finding to be one of the most significant results of this study.

It would be a mistake, however, to assume that all 3DBL features are controlled by the APG strains: another noteworthy characteristic of the swept-wing strain flow is illustrated in figure 19, concerning the early evolution of the spanwise Reynolds shear stress $-\overline{v'w'}$. The closely similar behaviour of the mean-gradient and shear-stress angles, γ_g and γ_τ, observed for Cases S45 and AS45 (cf. figures 8 and 19) points to the lack of dependence of $-\partial\,\overline{v'w'}/\partial t$ on the mean normal-strain components. In other words, the misalignment between $(\partial\,\overline{u}/\partial y, \partial\,\overline{w}/\partial y)$ and $(-\overline{u'v'}, -\overline{v'w'})$ is not affected by the mean deformation induced by the APG. The quantities that are responsible, and their insensitivity to the streamwise pressure gradient, are topics of the next subsection.

3.2.2. *Reynolds-stress budgets*

As in § 3.1.2, we begin with the turbulence kinetic energy k. The profiles in figure 20 reveal the origin of the increase observed in figure 17(*b*). Whereas the initial impact of the pure-skewing strain was negligible (cf. figure 9), for the swept-wing case the applied-strain production $P_k^{\mathscr{A}}$ (open symbols in figure 20*a*) instantly provides a substantial source of energy to the turbulence. (The thick solid curve in figure 20(*a*) represents the sum of $P_k^{\mathscr{A}}$ and the initial impulsive change to Π_k (the shaded region) caused by the immediate alteration of the pressure field produced by the applied strain;

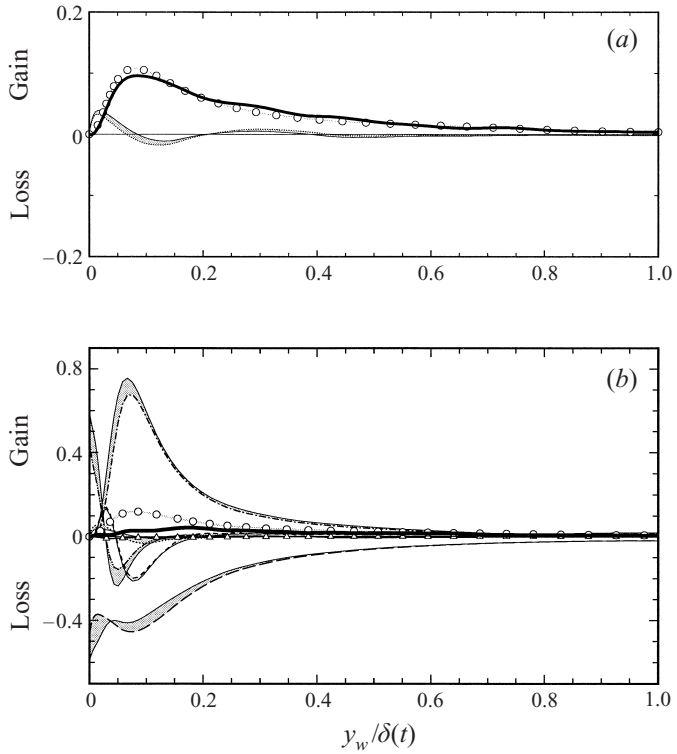

FIGURE 20. Terms in the budget of turbulence kinetic energy $k = 0.5\overline{u_i'u_i'}$ at (*a*) $\mathscr{A}_{13}t = 0$ and (*b*) $\mathscr{A}_{13}t = 0.125$ for Case AS45. Quantities in (*a*) are those instantly affected by applied strain: ——, $\Pi_k = \frac{1}{2}\Pi_{ii}$ for unstrained initial field; ·····, Π_k just after strain applied; ○, $-\overline{u'u'}\mathscr{A}_{11} - \overline{v'v'}\mathscr{A}_{22} - \overline{w'w'}\mathscr{A}_{33}$ (i.e. non-zero terms of applied-strain production $P_k^{\mathscr{A}} = \frac{1}{2}P_{ii}^{\mathscr{A}}$) at $\mathscr{A}_{13}t = 0$; ——, sum of all terms ($\approx \partial k/\partial t$) immediately after strain applied. Quantities in (*b*) reveal changes after finite time: thin solid curves (——) denote terms at $\mathscr{A}_{13}t = 0$ (before strain); —·—, P_k^S at $\mathscr{A}_{13}t = 0.125$; – – – –, $-\varepsilon_k$ at $\mathscr{A}_{13}t = 0.125$; - - - -, T_k at $\mathscr{A}_{13}t = 0.125$; —··—, D_k at $\mathscr{A}_{13}t = 0.125$; ·····, Π_k at $\mathscr{A}_{13}t = 0.125$; △, $-2\overline{u'w'}\mathscr{A}_{13}$ at $\mathscr{A}_{13}t = 0.125$; ○, $-\overline{u'u'}\mathscr{A}_{11} - \overline{v'v'}\mathscr{A}_{22} - \overline{w'w'}\mathscr{A}_{33}$ at $\mathscr{A}_{13}t = 0.125$; thick solid curve (——), sum of all terms ($\approx \partial k/\partial t$) at $\mathscr{A}_{13}t = 0.125$. Shaded regions indicate change from unstrained initial-condition profiles. Normalization as in figure 9. (Note difference in vertical scales of *a* and *b*.)

the Π_k change is much smaller than the initial $P_k^{\mathscr{A}}$.) The turbulence becomes more energetic for Case AS45 than for Case S45 because of the normal-strain components in the swept-wing field; since $P_k^{\mathscr{A}} = -2\overline{u'w'}\mathscr{A}_{13} - \overline{u'u'}\mathscr{A}_{11} - \overline{v'v'}\mathscr{A}_{22} - \overline{w'w'}\mathscr{A}_{33}$ (and the normal Reynolds stresses of the two-dimensional initial field are non-zero), the irrotational strain creates and maintains a production term that is of the order of 15–20% of the initial shear production P_k^S. The open circles in figure 20 denote the fraction of $P_k^{\mathscr{A}}$ defined by the streamwise $\mathscr{A}_{11}$, wall-normal $\mathscr{A}_{22}$, and spanwise $\mathscr{A}_{33}$ components while the open triangles correspond to that due to $\mathscr{A}_{13}$. (This convention will also be used for the other Reynolds stresses, with circles and triangles used to distinguish between applied-strain production $P_{ij}^{\mathscr{A}}$ associated with the normal and off-diagonal components, respectively.) The Case AS45 strain has a distinct implicit or indirect effect on the budget for k, since it leads to pronounced changes of all the terms present in the unstrained field (see the shaded regions in figure 20*b*). For example, the large structural alteration illustrated above by the turbulent transport velocity V_{q^2} (figure 18*b*) appears in figure 20 as the difference between the initial and $\mathscr{A}_{13}t = 0.125$ (short-

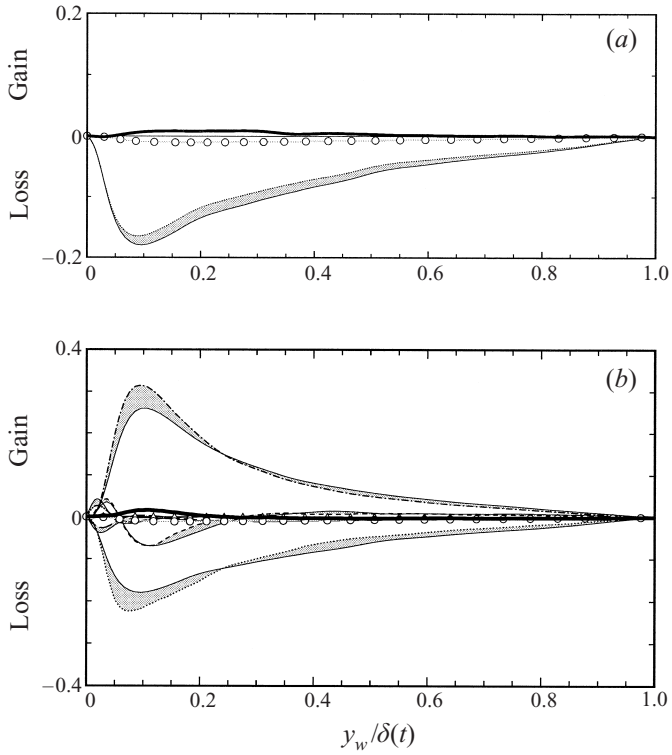

FIGURE 21. Terms in the budget of streamwise Reynolds shear stress $-\overline{u'v'}$ at (*a*) $\mathscr{A}_{13}t = 0$ and (*b*) $\mathscr{A}_{13}t = 0.125$ for Case AS45. Quantities in (*a*) are those instantly affected by applied strain: ——, $-\Pi_{12}$ for unstrained initial field; · · · · · ·, $-\Pi_{12}$ just after strain applied; ○, $\overline{u'v'}(\mathscr{A}_{11} + \mathscr{A}_{22})$ (i.e. non-zero terms of applied-strain production $-P_{12}^{\mathscr{A}}$) at $\mathscr{A}_{13}t = 0$; ——, sum of all terms ($\approx -\partial\overline{u'v'}/\partial t$) immediately after strain applied. Quantities in (*b*) reveal changes after finite time: thin solid curves (——) denote terms at $\mathscr{A}_{13}t = 0$ (before strain); —·—, $-P_{12}^{S}$ at $\mathscr{A}_{13}t = 0.125$; – – – –, $+\varepsilon_{12}$ at $\mathscr{A}_{13}t = 0.125$; - - - -, $-T_{12}$ at $\mathscr{A}_{13}t = 0.125$; —··—, $-D_{12}$ at $\mathscr{A}_{13}t = 0.125$; · · · · · ·, $-\Pi_{12}$ at $\mathscr{A}_{13}t = 0.125$; △, $\overline{v'w'}\mathscr{A}_{13}$ at $\mathscr{A}_{13}t = 0.125$; ○, $\overline{u'v'}(\mathscr{A}_{11} + \mathscr{A}_{22})$ at $\mathscr{A}_{13}t = 0.125$; thick solid curve (——), sum of all terms ($\approx -\partial\overline{u'v'}/\partial t$) at $\mathscr{A}_{13}t = 0.125$. Shaded regions indicate change from unstrained initial-condition profiles. Normalization as in figure 9. (Note difference in vertical scales of *a* and *b*.)

dashed) turbulent transport curves T_k; changes to the shear production, dissipation, viscous diffusion, and velocity–pressure-gradient terms are even larger. Nevertheless, the explicit contribution of $P_k^{\mathscr{A}}$ is larger still. It leads to positive $\partial k/\partial t$ at every y_w location, and thus accounts for the uniform increase of the k profiles found in figure 17(*b*), and the rising history in figure 16(*c*). In the sense of being able to directly supply energy to the turbulence, the APG-induced strains (diagonal components) therefore have a more profound influence on the flow than the $\mathscr{A}_{13}$ skewing does.

The explanation is less straightforward for the $-\overline{u'v'}$ budget, whose terms are shown in figure 21. Instead of being mostly the result of the applied-strain production, the sign of the initial $-\partial\,\overline{u'v'}/\partial t$ pulse (the thick solid curve in figure 21*a*) is now determined by an immediate increase of $-\Pi_{12}$ (the shaded region) due to the initial step change of the pressure field as it responds to the application of the strain. The figure 21(*b*) results indicate that the same tendency, for $-\partial\,\overline{u'v'}/\partial t$ and $-P_{12}^{\mathscr{A}}$ to be of opposite sign, is also found after finite time ($\mathscr{A}_{13}t = 0.125$). The indirect effect of the strain is thus more important in the development of $-\overline{u'v'}$ than are either of

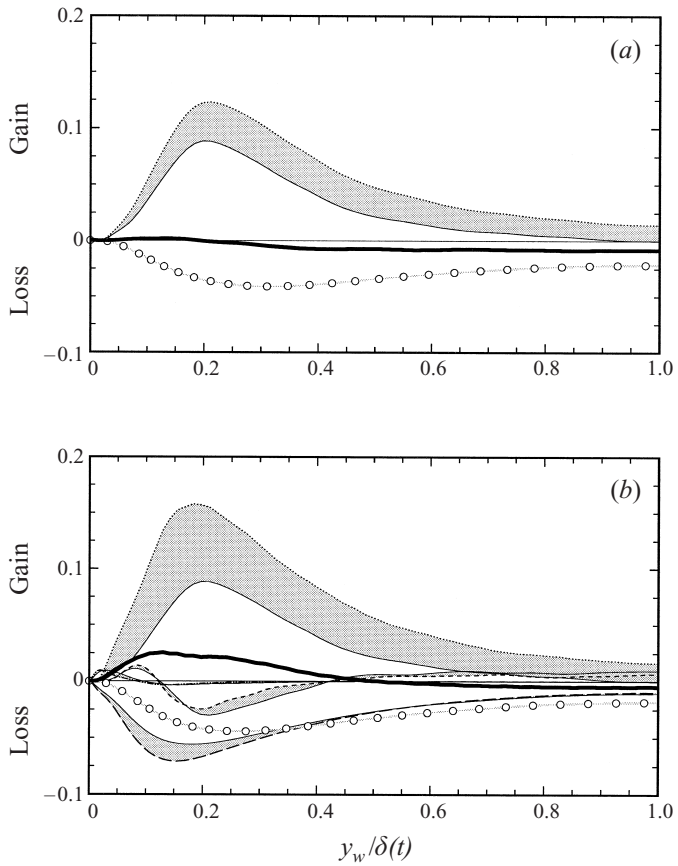

FIGURE 22. Terms in the budget of vertical-velocity variance $\overline{v'v'}$ at (*a*) $\mathscr{A}_{13}t = 0$ and (*b*) $\mathscr{A}_{13}t = 0.125$ for Case AS45: Quantities in (*a*) are those instantly affected by applied strain: ——, velocity–pressure-gradient correlation Π_{22} for unstrained initial field; · · · · · ·, Π_{22} just after strain applied; ○, $P_{22}^{\mathscr{A}} = -2\overline{v'v'}\mathscr{A}_{22}$ at $\mathscr{A}_{13}t = 0$; ——, sum of all terms ($\approx \partial\overline{v'v'}/\partial t$) immediately after strain applied. Quantities in (*b*) reveal changes after finite time: thin solid curves (——) denote terms at $\mathscr{A}_{13}t = 0$ (before strain); – – – –, $-\varepsilon_{22}$ at $\mathscr{A}_{13}t = 0.125$; - - - -, T_{22} at $\mathscr{A}_{13}t = 0.125$; — · · —, D_{22} at $\mathscr{A}_{13}t = 0.125$; · · · · · ·, Π_{22} at $\mathscr{A}_{13}t = 0.125$; ○, $P_{22}^{\mathscr{A}}$ at $\mathscr{A}_{13}t = 0.125$; thick solid curve (——), sum of all terms ($\approx \partial\overline{v'v'}/\partial t$) at $\mathscr{A}_{13}t = 0.125$. Shaded regions indicate change from unstrained initial-condition profiles. Normalization as in figure 9.

the normal or off-diagonal contributions to the applied-strain production $-P_{12}^{\mathscr{A}}$. The positive $-\partial\,\overline{u'v'}/\partial t$ found at $\mathscr{A}_{13}t = 0.125$ is primarily due to the imbalance between two large changes: an increase in the shear production $-P_{12}^{s}$, and a decrease in the velocity–pressure-gradient correlation $-\Pi_{12}$, with the former slightly larger than the latter. (Note that in the outer layer, both the initial-impulse and $\mathscr{A}_{13}t = 0.125$ values of $-\Pi_{12}$ represent a source of $-\overline{u'v'}$, while below $y_w = 0.3\delta(t)$ this term also begins as a source but eventually acts to reduce the $-\overline{u'v'}$ stress.) The amplification of the shear production $-P_{12}^{s} = \overline{v'v'}\partial\,\overline{u}/\partial y$ is itself a symptom of a significant change to Π_{22}, another of the velocity–pressure-gradient components. The growth of $-P_{12}^{s}$ is caused by growth of the vertical-velocity variance $\overline{v'v'}$. (Recall that figure 16 indicates a $\partial\,\overline{u}/\partial y$ decrease in the immediate vicinity of the wall.) Figure 22 shows that the $\overline{v'v'}$ increase is primarily the result of strain-induced alterations to Π_{22}. Once again the initial impulsive change to the velocity–pressure-gradient correlation acts to instantly

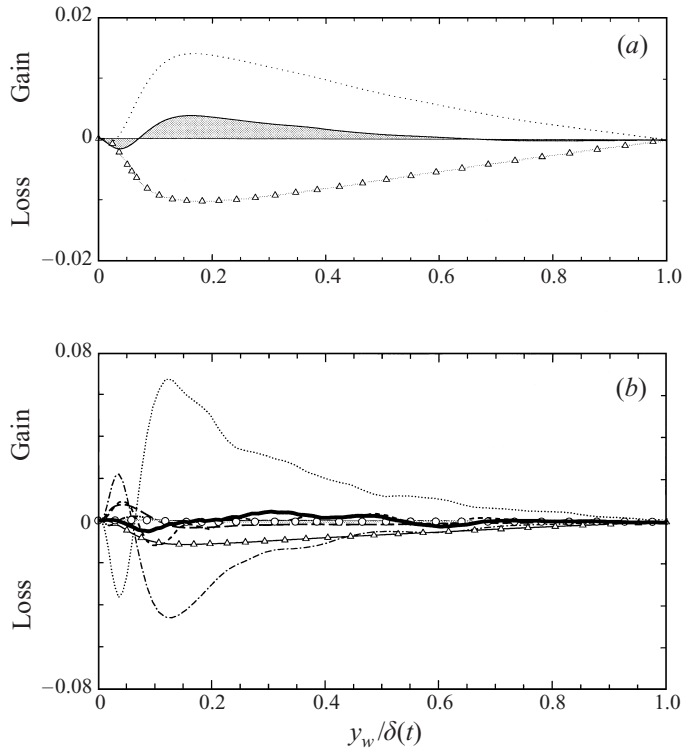

FIGURE 23. Terms in the budget of spanwise Reynolds shear stress $-\overline{v'w'}$ for Case AS45 at (*a*) $\mathscr{A}_{13}t = 0$ (immediately after swept-wing strain applied) and (*b*) $\mathscr{A}_{13}t = 0.125$ for Case AS45: —·—, $-P^S_{23}$; ————, $+\varepsilon_{23}$; - - - -, $-T_{23}$; —··—, $-D_{23}$; ·····, $-\Pi_{23}$; △, $\overline{u'v'}\mathscr{A}_{13}$; ○, $\overline{v'w'}(\mathscr{A}_{22} + \mathscr{A}_{33})$; thick solid curve (——), sum of all terms ($\approx -\partial\overline{v'w'}/\partial t$) at $\mathscr{A}_{13}t = 0.125$. Solid curve (——) and shaded region in (*a*) indicate net imbalance initially supplied by sum of $-P^{\mathscr{A}}_{23}$ and $-\Pi_{23}$ (i.e. the terms instantly affected by applied strain); unstrained initial-field profile subtracted from $-\Pi_{23}$ in (*a*) to remove statistically insignificant oscillations. (Note difference in vertical scales of *a* and *b*.) Normalization as in figure 9.

offset the applied-strain production, with the Π_{22} increase roughly balancing the negative $P^{\mathscr{A}}_{22}$ first applied to the flow (figure 22*a*); at later times, Π_{22} overwhelms the explicit production, causing the net positive $\partial\overline{v'v'}/\partial t$ observed in figure 22(*b*), which in turn leads to the $-\overline{u'v'}$ and k growth evident in the above statistics. This behaviour is absent from Case S45. Neither the explicit $\overline{v'v'}$ production $P^{\mathscr{A}}_{22} = -2\overline{v'v'}\mathscr{A}_{22}$ (which here represents a sink, since $\mathscr{A}_{22} > 0$) nor the Π_{22} 'kickback' is present when the skewing deformation acts alone (cf. figure 12). An APG is needed to thicken the layer (or a favourable one needed to thin it) for this Π_{22}-versus-$P^{\mathscr{A}}_{22}$ imbalance to occur.

Our last result concerns the $-\overline{v'w'}$ budget, presented in figure 23. It reveals yet another 'tug-of-war' (partial cancellation) between the implicit effects embodied by the velocity–pressure-gradient term ($-\Pi_{23}$) and explicit new production supplied by mean flow gradients, in this case by both the spanwise shear ($\overline{v'v'}\,\partial\,\overline{w}/\partial y$) and the applied strain ($\overline{u'v'}\mathscr{A}_{13} + \overline{v'w'}[\mathscr{A}_{22} + \mathscr{A}_{33}]$). Immediately after the strain is applied, the impact of the swept-wing deformation is nearly identical to that of the pure-skewing strain. This is because $-\overline{v'w'}$ is zero for a two-dimensional flow,† so that $-P^{\mathscr{A}}_{23}$ is initially the

† The extent to which this infinite-ensemble-average idealization is realized by the initial fields is revealed by the solid curves in figures 8(*b*) and 19(*b*).

same for the two cases, and because the normal-strain components have a negligible effect on the initial $-\Pi_{23}$ jump created by the impulsive distortion. The latter can be inferred by comparing the dotted curves in figures 13(*a*) and 23(*a*), which respectively indicate the impulsive initial changes of $-\Pi_{23}$ for Cases S45 and AS45; they are indistinguishable. The budgets are also qualitatively similar even after the turbulence has been subjected to the two strain fields for a finite time, with the $-P^{s}_{23}$ and $-P^{\mathscr{A}}_{23}$ production, the $-\Pi_{23}$ correlation, and net $-\partial\,\overline{v'w'}/\partial t$ each in approximately the same proportion, regardless of whether or not the normal-strain components are active (cf. figures 13*b* and 23*b*). In the light of this similarity, it is no surprise that the shear-stress angle γ_τ profiles in figures 8(*b*) and 19(*b*) agree so well. Once again we notice that the magnitude of the net $-\partial\,\overline{v'w'}/\partial t$ is given by the difference of much larger terms.

The $-\overline{v'w'}$ budgets for Cases AS45 and S45 have at least two significant implications. The first is simply that this component of shear stress is primarily affected by the $\mathscr{A}_{13}$ skewing (either directly or indirectly) and the mean spanwise shear that the skewing generates; in 3DBLs of practical interest, $-\overline{v'w'}$ (and the lag between the mean-shear and shear-stress angles γ_g and γ_τ) is therefore likely to be relatively insensitive to the normal-strain components introduced by adverse pressure gradients. A second, broader, implication of the budget analysis is the need to capture the effect of each of the velocity–pressure-gradient terms in turbulence models used to predict the development of suddenly distorted three-dimensional boundary layers.

4. Summary and concluding remarks

Time-developing strained-channel flow has been simulated as an idealization of pressure-driven three-dimensional turbulent boundary layers. DNS results are used to investigate questions regarding the physics and modelling of three-dimensional wall layers that arise from sudden mean-flow perturbations. This approach has the advantage of capturing the essential features of perturbed 3DBLs with a turbulent flow whose statistics depend only on time and one spatial dimension. Several of the difficult-to-model characteristics found in the spatial case are observed and quantified. These include the lag between the mean shear and Reynolds shear stress, the modification of the relationship between the components of the Reynolds stress tensor, and the controlling influence of the pressure–velocity correlation terms in the Reynolds-stress budgets.

Two strain fields were considered, with and without the effect of streamwise deceleration, but both including the same mean skewing components. The flow histories reveal that the impact of the APG on the outer-layer structure of the turbulence is more profound than that of the mean three-dimensionality. The stress/energy ratio a_1 experiences a much larger decrease when the APG strain is present. Although the strain rate used here is larger than that imposed in 3DBL experiments in which the stress/energy ratio decrease was attributed to mean crossflow (e.g. van den Berg *et al.* 1975; Bradshaw & Pontikos 1985; Schwarz & Bradshaw 1994), the dominance of the APG over the skewing deformation appears to be a fairly general result. Gleyzes *et al.* (1993) found that the same conclusion holds in the boundary layer over a finite swept wing, while Webster *et al.* (1996) have more recently discovered that the APG overwhelms the influence of the skewing in their experimental study of the three-dimensional boundary layer over a swept bump. While significant structural changes effected solely by spanwise shear are well-documented for purely shear-driven 3DBLs (e.g. Driver & Hebbar 1987; Moin *et al.* 1990; Jung *et al.* 1992; Le *et al.* 1999), it appears that $\partial\,\overline{w}/\partial y$-induced changes in the outer layer are modest.

Nearer to the wall the story is different. Here the effect of the spanwise shear is crucial, for both the shear- and pressure-driven cases. This can be inferred for example by the common near-wall kinetic energy reduction observed in the shear-driven three-dimensional channel flows (Moin *et al.* 1990; Coleman *et al.* 1996*a*; and Le *et al.* 1999), the strained channel (Case S45 and the low-strain-rate version of Case AS45) discussed above, and the infinite-swept-wing experiment of Bradshaw & Pontikos (1985). It is significant that the pure-skewing Case S45 results demonstrate the stabilizing behaviour associated with conversion of a two-dimensional stationary boundary layer to a non-stationary one by addition of shear-generated mean three-dimensionality. The similarity of the near-wall dynamics of shear- and pressure-driven 3DBLs becomes even more apparent when the Reynolds-stress budgets for the pure-skewing and spanwise-moving-wall channel flows are compared (see figures 3 and 4 of Le *et al.* 1999).

In addition to producing the above general conclusions, the DNS results can be used in a quantitative manner to test and develop specific Reynolds-averaged closures. Data files containing the drag histories, mean and variance profiles, and Reynolds-stress budgets presented here are available from the authors for this purpose. To aid in this endeavour, the channel-flow solver of Wilcox (1998) has been modified to accommodate the strained-channel geometry and will be supplied upon request (Fortran and C versions are available). In addition to this code, which should be useful to modellers interested in testing their schemes against the DNS statistics, benchmark data have also been prepared by applying the strains to the laminar channel flow; these will allow rapid validation of the moving-wall boundary conditions and straining terms needed for the conversion of conventional- to strained-channel solvers.

This work was sponsored by the Office of Naval Research (Grant No. N00014-94-1-0016), Dr L. P. Purtell program officer. It was done in collaboration with Dr A.-T. Le. Computer resources have been supplied by the NAS program at NASA-Ames Research Center, the San Diego Supercomputer Center NPACI program, and the DOD Major Shared Resource Center. The C version of the strained-channel model-test program was converted from Fortran by Mr Khaled Nefti. At various stages of this study we have benefited from insightful comments and suggestions made by Professor P. Bradshaw.

Appendix. Numerical procedures

The deforming coordinate system (2.9*a*) results in momentum and continuity equations that are very similar to those governing conventional Poiseuille flow. Because of this similarity, we are able to benefit from previous code development and testing, and construct an accurate and efficient solver by making straight-forward alterations to a well-established algorithm.

The conversion begins by recasting (2.10) into the (v, ω_y) formulation employed by Kim *et al.* For the present flow we write

$$\frac{\partial}{\partial \widehat{t}}\widehat{\nabla}^2 v^* = \widehat{h}_v + \frac{1}{Re}\widehat{\nabla}^2(\widehat{\nabla}^2 v^*), \tag{A 1a}$$

$$\frac{\partial \widehat{g}}{\partial \widehat{t}} = \widehat{h}_g + \frac{1}{Re}\widehat{\nabla}^2 \widehat{g}, \tag{A 1b}$$

$$\widehat{f} + \mathscr{B}_{22}\frac{\partial v^*}{\partial \xi_2} = 0, \tag{A 1c}$$

where $\hat{g} = \hat{\omega}_2$ is the wall-normal component of vorticity, $\hat{\omega}_i = \epsilon_{ij\ell}\mathscr{B}_{nj}\partial u^*_\ell/\partial\xi_n$, and

$$\hat{\nabla}^2(\ ) = \mathscr{B}_{11}^2\frac{\partial^2(\ )}{\partial\xi_1\partial\xi_1} + \mathscr{B}_{22}^2\frac{\partial^2(\ )}{\partial\xi_2\partial\xi_2} + \mathscr{B}_{33}^2\frac{\partial^2(\ )}{\partial\xi_3\partial\xi_3},$$

with

$$\hat{f} = \mathscr{B}_{11}\frac{\partial u^*}{\partial\xi_1} + \mathscr{B}_{33}\frac{\partial w^*}{\partial\xi_3}, \qquad \hat{g} = \mathscr{B}_{33}\frac{\partial u^*}{\partial\xi_3} - \mathscr{B}_{11}\frac{\partial w^*}{\partial\xi_1}, \tag{A 1d}$$

$$\begin{aligned}\hat{h}_v = &-\mathscr{B}_{22}\frac{\partial}{\partial\xi_2}\left(\mathscr{B}_{11}\frac{\partial\hat{H}_1}{\partial\xi_1} + \mathscr{B}_{33}\frac{\partial\hat{H}_3}{\partial\xi_3}\right) + \mathscr{B}_{11}^2\frac{\partial^2\hat{H}_2}{\partial\xi_1\partial\xi_1} + \mathscr{B}_{33}^2\frac{\partial^2\hat{H}_2}{\partial\xi_3\partial\xi_3}\\ &+\mathscr{B}_{22}\frac{\partial}{\partial\xi_2}\left(\mathscr{B}_{11}\mathscr{A}^*_{11}\frac{\partial u^*}{\partial\xi_1} + \mathscr{B}_{33}\mathscr{A}^*_{33}\frac{\partial w^*}{\partial\xi_3}\right)\\ &-2\mathscr{B}_{11}^2\mathscr{A}^*_{11}\frac{\partial^2 v^*}{\partial\xi_1\partial\xi_1} - \mathscr{B}_{22}^2\mathscr{A}^*_{22}\frac{\partial^2 v^*}{\partial\xi_2\partial\xi_2} - 2\mathscr{B}_{33}^2\mathscr{A}^*_{33}\frac{\partial^2 v^*}{\partial\xi_3\partial\xi_2},\end{aligned} \tag{A 1e}$$

$$\hat{h}_g = \mathscr{B}_{33}\frac{\partial\hat{H}_1}{\partial\xi_3} - \mathscr{B}_{11}\frac{\partial\hat{H}_3}{\partial\xi_1} - \mathscr{B}_{33}\mathscr{A}^*_{33}\frac{\partial u^*}{\partial\xi_3} + \mathscr{B}_{11}\mathscr{A}^*_{11}\frac{\partial w^*}{\partial\xi_1}, \tag{A 1f}$$

and

$$\hat{H}_i = -\left.\frac{\partial\overline{p}}{\partial x_i^*}\right|_{\text{app}} + \epsilon_{ijk}u^*_j\hat{\omega}_k - u^*_j\mathscr{A}^*_{ij}. \tag{A 1g}$$

Equation (A 1) is equivalent to Kim *et al.*'s equations (3)–(5), except for the new terms involving the applied strain $\mathscr{A}^*_{ij}$, and the time-dependent metric $\mathscr{B}_{ij}(\hat{t}\,) = \exp(-\mathscr{A}^*_{ij}\hat{t}\,)$ multiplying each spatial derivative.

We can utilize the Kim *et al.* algorithm simply by replacing their dependent variables $\nabla^2 v$ and g with $\hat{\nabla}^2 v^*$ and $\hat{g}$, with the understanding that their time and spatial derivatives $\partial(\ )/\partial t$ and $\partial(\ )/\partial x_i$ now correspond respectively to $\partial(\ )/\partial\hat{t}$ and $\mathscr{B}_{ji}\partial(\ )/\partial\xi_j$, and $\nabla^2(\ ) \leftarrow \hat{\nabla}^2(\ )$, $h_v \leftarrow \hat{h}_v$, $h_g \leftarrow \hat{h}_g$, and $H_i \leftarrow \hat{H}_i$. Actual coding changes therefore involve multiplying all spatial derivatives by the appropriate explicit time-dependent function $\mathscr{B}_{ij}(\hat{t}\,)$ (with attention paid to the elapsed time, and an appropriate distinction between spatial derivatives associated with 'previous', 'current', and 'upcoming' timesteps), and adding the $\mathscr{A}_{ij}$ terms to h_v, h_g, and the convective term H_i. The latter requires modification of the CFL number definition, as in Blaisdell, Mansour & Reynolds (1991).

The other major change is to the wall-boundary conditions, to allow the non-zero in-plane motion $\boldsymbol{u}^*_w$ prescribed by (2.14). This requires monitoring the initial and current mean centreline velocity, and saving the initial values during stops and restarts of the code.

All other characteristics of the solution procedure are identical to those detailed in Kim *et al.* (1987).

REFERENCES

Alving, A. E. & Fernholz, H. H. 1995 Mean-velocity scaling in and around a mild, turbulent separation bubble. *Phys. Fluids* **7**, 1956–1969.

Anderson, S. D. & Eaton, J. K. 1989 Reynolds stress development in pressure-driven three-dimensional turbulent boundary layers. *J. Fluid Mech.* **202**, 263–294.

Berg, B. van den, Elsenaar, A., Lindhout, J. P. F. & Wesseling, P. 1975 Measurements in an incompressible three-dimensional turbulent boundary layer, under infinite swept-wing conditions, and comparison with theory. *J. Fluid Mech.* **70**, 127–148.

Berg, B. van den, Humphreys, D. A., Krause, E. & Lindhout, J. P. F. 1988 *Three-Dimensional Turbulent Boundary Layers – Calculations and Experiments*. Notes on Numerical Fluid Mechanics, vol. 19. Vieweg & Sohn.

Blaisdell, G. A., Mansour, N. N. & Reynolds, W. C. 1991 Numerical simulation of compressible homogeneous turbulence. *Dept. of Mech. Engng, Stanford University, Thermosciences Div. Rep.* TF-50.

Bradshaw, P. 1987 Turbulent secondary flows. *Ann. Rev. Fluid Mech.* **19**, 53–74.

Bradshaw, P. & Pontikos, N. S. 1985 Measurements in the turbulent boundary layer on an 'infinite' swept wing. *J. Fluid Mech.* **159**, 105–130.

Coleman, G. N. 1999 Similarity statistics from a direct numerical simulation of the neutrally stratified planetary boundary layer. *J. Atmos. Sci.* **56**, 891–900.

Coleman, G. N., Ferziger, J. H. & Spalart, P. R. 1990 A numerical study of the turbulent Ekman layer. *J. Fluid Mech.* **213**, 313–348.

Coleman, G. N., Kim, J. & Le, A.-T. 1996*a* A numerical study of three-dimensional wall-bounded flows. *Intl J. Heat Fluid Flow* **17**, 333–342.

Coleman, G. N., Kim, J. & Spalart, P. R. 1996*b* Direct numerical simulation of strained three-dimensional wall-bounded flows. *Expl Thermal Fluid Sci.* **13**, 239–251.

Coleman, G. N., Kim, J. & Spalart, P. R. 1997 Direct numerical simulation of decelerated wall-bounded shear flows. *Eleventh Symp. on Turbulent Shear Flows*, Grenoble, France, September 8–10, 1997.

Driver, D. M. & Hebbar, S. K. 1987 Experimental study of a three-dimensional, shear-driven, turbulent boundary layer. *AIAA J.* **25**, 35–42.

Driver, D. M. & Hebbar, S. K. 1991 Three-dimensional turbulent boundary layer flow over a spinning cylinder. *NASA Tech. Memo.* 102240.

Eaton, J. K. 1995 Effects of mean flow three dimensionality on turbulent boundary-layer structure. *AIAA J.* **33**, 2020–2025.

Fernholz, H. H. & Vagt, J.-D. 1981 Turbulence measurements in an adverse-pressure-gradient three-dimensional turbulent boundary layer along a circular cylinder. *J. Fluid Mech.* **111**, 233–269.

Furuya, Y., Nakamura, I. & Kawachi, H. 1966 The experiment on the skewed boundary layer on a rotating body. *Bull. Japan Soc. Mech. Engng* **9**, 702–710.

Flack, K. A. & Johnston, J. P. 1993 Near-wall investigation of three-dimensional turbulent boundary layers. *Dept. of Mech. Engng, Stanford University, Thermosciences Div. Rep.* MD-63.

Gleyzes, C., Maciel, Y., Cousteix, J., Gooden, J. H. M., Reinders, W., Berg, B. van den 1993 Three-dimensional turbulent flow around the Garteur swept wing. In *Ninth Symp. on Turbulent Shear Flows*, *Kyoto*, *Japan*, *August 16–18, 1993.*

Hawthorne, W. R. 1951 Secondary circulation in fluid flow. *Proc. R. Soc. Lond.* A **206**, 374–387.

Hawthorne, W. R. 1954 The secondary flow about struts and airfoils. *J. Aeronaut. Sci.* **21**, 588–608.

Howard, R. J. A. & Sandham, N. D. 1996 Simulation and modelling of the skew response of turbulent channel flow to spanwise flow deformation. In *Second ERCOFTAC Workshop on Direct and Large-Eddy Simulation, Grenoble, France, September 14–18, 1996.*

Johnston, J. P. & Flack, K. A. 1996 Review of advances in three-dimensional turbulent boundary layers with emphasis on the wall-layer regions. *Trans. ASME*: *J. Fluids Engng* **118**, 219–232.

Jung, W. J., Mangiavacchi, N. & Akhavan, R. 1992 Suppression of turbulence in wall-bounded flows by high-frequency spanwise oscillations. *Phys. Fluids* A **4**, 1605–1607.

Kang, H. S., Choi, H. & Yoo, J. Y. 1998 On the modification of the near-wall coherent structure in a three-dimensional turbulent boundary layer on a free rotating disk. *Phys. Fluids* **10**, 2315–2322.

Kiesow, R. Q. & Plesniak, M. W. 1999 Modification of near-wall structure in a three-dimensional turbulent boundary layer. In *First Symp. on Turbulence and Shear Flow Phenomena, University of California, Santa Barbara, USA, September 13–15, 1999.*

Kim, J., Moin, P. & Moser, R. 1987 Turbulence statistics in fully developed channel flow at low Reynolds number. *J. Fluid Mech.* **177**, 133–166.

Laadhari, F., Skandaji, L. & Morel, R. 1994 Turbulence reduction in a boundary layer by a local spanwise oscillating surface. *Phys. Fluids* **6**, 3218–3220.

Lanczos, C. 1956 *Applied Analysis*. Prentice-Hall.

Le, A.-T. 1999 A numerical study of three-dimensional boundary layers. PhD thesis, University of California, Los Angeles.

Le, A.-T., Coleman, G. N. & Kim, J. 1999 Near-wall turbulence structures in three-dimensional boundary layers. In *First Symp. on Turbulence and Shear Flow Phenomena, University of California, Santa Barbara, USA, September 13–15, 1999*.

Lee, M. J. & Reynolds, W. C. 1985 Numerical experiments on the structure of homogeneous turbulence. *Dept. of Mech. Engng, Stanford University, Thermosciences Div. Rep.* TF-24.

Littel, H. S. & Eaton, J. K. 1994 Turbulence characteristics of the boundary layer on a rotating disk. *J. Fluid Mech.* **266**, 175–207.

Lohmann, R. P. 1976 The response of a developed turbulent boundary layer to local transverse surface motion. *Trans. ASME*: *J. Fluids Engng* **98**, 354–363.

Mansour, N. N., Kim, J. & Moin, P. 1988 Reynolds-stress and dissipation-rate budgets in a turbulent channel flow. *J. Fluid Mech.* **194**, 15–44.

Moin, P., Shih, T.-H., Driver, D. M. & Mansour, N. N. 1990 Direct numerical simulation of a three-dimensional turbulent boundary layer. *Phys. Fluids* A **2**, 1846–1853.

Nagano, Y., Tagawa, M. & Tsuji, T. 1991 Effects of adverse pressure gradients on mean flows and turbulence statistics in a boundary layer. In *Eighth Symp. on Turbulent Shear Flows, Munich, Germany, September 9–11, 1991*.

Ölçmen, S. M. & Simpson, R. L. 1995 An experimental study of a three-dimensional pressure-driven turbulent boundary layer. *J. Fluid Mech.* **290**, 225–262.

Pierce, F. J. & Duerson, S. H. Jr. 1975 Reynolds stress tensors in an end-wall three-dimensional channel boundary layer. *Trans. ASME*: *J. Fluids Engng* **97**, 618–620.

Rogallo, R. S. 1981 Numerical experiments in homogeneous turbulence. *NASA Tech. Memo*. 81315. Available from NASA Scientific & Technical Information (help@sti.nasa.gov).

Rogers, M. M. 2000 The evolution of strained turbulent plane wakes. *J. Fluid Mech.* (accepted).

Schwarz, W. R. & Bradshaw, P. 1994 Turbulence structural changes for a three-dimensional turbulent boundary layer in a 30° bend. *J. Fluid Mech.* **272**, 183–209.

Sendstad, O. & Moin, P. 1992 The near wall mechanics of three-dimensional turbulent boundary layers. *Dept. of Mech. Engng, Stanford University, Thermosciences Div. Rep.* TF-57.

Smits, A. J. & Wood, D. H. 1985 The response of turbulent boundary layers to sudden perturbations. *Ann. Rev. Fluid Mech.* **17**, 321–358.

Spalart, P. R. 1989 Theoretical and numerical study of a three-dimensional turbulent boundary layer. *J. Fluid Mech.* **205**, 319–340.

Spalart, P. R. & Coleman, G. N. 1997 Numerical study of a separation bubble with heat transfer. *Eur. J. Mech.* B/*Fluids* **16**, 169–189.

Spalart, P. R., Moser, R. D. & Rogers, M. M. 1991 Spectral methods for the Navier–Stokes equations with one infinite and two periodic directions. *J. Comput. Phys.* **96**, 297–324.

Spalart, P. R. & Watmuff, J. H. 1993 Experimental and numerical study of a turbulent boundary layer with pressure gradients. *J. Fluid Mech.* **249**, 337–371.

Squire, H. B. & Winter, K. G. 1951 The secondary flow in a cascade of airfoils in a nonuniform stream. *J. Aeronaut. Sci.* **18**, 271–277.

Webster, D. R., DeGraaff, D. B. & Eaton, J. K. 1996 Turbulence characteristics of a boundary layer over a swept bump. *J. Fluid Mech.* **323**, 1–22.

Wilcox, D. C. 1998 *Turbulence Modeling for CFD*. DCW Industries (www.dcwindustries.com).

Wu, X. & Squires, K. D. 1997 Large eddy simulation of an equilibrium three-dimensional turbulent boundary layer. *AIAA J.* **35**, 67–74.